



^{99m}Tc -labeled keratin gold-nanoparticles in a nephron-like microfluidic chip for photo-thermal therapy applications



V. Frantellizzi ^{a,1}, V. Verrina ^{b,1}, C. Raso ^{b,1}, M. Pontico ^a, F. Petronella ^c, V. Bertana ^d, A. Ballesio ^d, S.L. Marasso ^{d,e}, S. Miglietta ^f, P. Rosa ^b, S. Scibetta ^b, V. Petrozza ^b, M.S. De Feo ^a, G. De Vincentis ^a, A. Calogero ^b, R. Pani ^b, G. Perotto ^g, L. De Sio ^{b,h,*}

^a Department of Radiological Sciences, Oncology and Anatomical Pathology, Sapienza University of Rome, Viale Regina Elena 324, 00161, Rome, Italy

^b Department of Medico-Surgical Sciences and Biotechnologies - Research Center for Biophotonics, Sapienza University of Rome, Corso della Repubblica 79, 04100 Latina, Italy

^c Institute of Crystallography CNR-IC, National Research Council of Italy, Via Salaria Km 29, 300, 00015 Monterotondo, Rome, Italy

^d Chilab-Materials and Microsystems Laboratory, Department of Applied Science and Technology (DISAT), Politecnico Di Torino, Via Lungo Piazza d'Armi 6, 10034 Chivasso (Turin), Italy

^e Institute of Materials for Electronics and Magnetism, IMEM-CNR, Parco Area delle Scienze 37/A, 43124 Parma, Italy

^f Department of Anatomy, Histology, Forensic Medicine and Orthopaedics, Sapienza University of Rome, Rome, Italy

^g Smart Materials, Istituto Italiano di Tecnologia, via Morego 30, 16163 Genoa, Italy

^h CNR-Lab. Licryl, Institute NANOTEC, Arcavacata di Rende, 87036, Italy

ARTICLE INFO

Article history:

Received 19 June 2022

Received in revised form

9 August 2022

Accepted 13 August 2022

Available online xxx

Keywords:

Biomimetic gold nanoparticles

Radiolabeling

Lab-on-a-chip

Animal-free

Radioimaging

Photo-thermal therapy

Theranostics

ABSTRACT

Biocompatible gold nanoparticles (AuNPs) are particularly interesting for photo-thermal therapy (PTT) of cancer treatment because of their ability to convert light into heating efficiently. Nevertheless, the random accumulation of AuNPs in tissues, mainly determined by their retention time in the bloodstream, is one of the main limiting factors for their use in PTT applications. For this reason, efficient targeting and monitoring of AuNPs in the selected tissues is of paramount importance. This manuscript reports on a new generation of ^{99m}Tc -labeled AuNPs coated with keratin (Ker-AuNPs) and their spatial localization investigated by nuclear imaging techniques on an animal-free model. The effective radiolabeling of Ker-AuNPs with ^{99m}Tc is achieved using the chelating agent diethylenetriaminepentaacetic acid (DTPA), resulting in the ^{99m}Tc -DTPA-Ker-AuNPs nanoconjugate. The ^{99m}Tc -DTPA-Ker-AuNPs display a radiochemical purity of 90.7% and excellent photo-thermal properties. In addition, the biocompatibility of the ^{99m}Tc -DTPA-Ker-AuNPs with healthy human embryonic kidney (HEK293T) cells is shown. A Lab-On-a-Chip (LoC) approach is used to localize and study the stability of ^{99m}Tc -DTPA-Ker-AuNPs under dynamic conditions. To this end, the nanoconjugates are injected into a polydimethylsiloxane microfluidic chip mimicking the renal filtering unit, the nephron, and monitored via radio-imaging and thermo-optical experiments. These detailed studies establish that DTPA-assisted ^{99m}Tc -labeled Ker-AuNPs are excellent candidates as biocompatible and non-invasive radiolabeled nanotherapeutic for PTT-based applications.

© 2022 The Authors. Published by Elsevier Ltd. This is an open access article under the CC BY-NC-ND license (<http://creativecommons.org/licenses/by-nc-nd/4.0/>).

1. Introduction

The use of gold nanoparticles (AuNPs) for innovative biomedical applications has been extensively studied in recent decades [1–6]. It has been reported that AuNPs can be used in several medical

applications such as diagnostics, therapy, prevention, hygiene, and drug delivery [7–12]. The optical properties of AuNPs are determined by their local surface plasmon resonance (LSPR) [13,14], which is associated with the collective excitation of conduction electrons (localised on the AuNPs surface), resulting in intense absorption plasmon bands (plasmons). Plasmons can be located in a broad region of the electromagnetic spectrum (from the visible to the near-infrared (NIR) region), depending on the AuNP size, shape, and surrounding refractive index [15,16].

The possibility of combining AuNPs with biomaterials such as

* Corresponding author.

E-mail address: luciano.desio@uniroma1.it (L. De Sio).

¹ These authors contributed equally to this paper.

biomolecules, polymers, and proteins has been intensively explored [17–20]. This powerful combination enables the realization of functionalized AuNPs with improved biocompatibility, bio-distribution, and stability.

Arabic gum, serum albumin, and keratin are the most common proteins used because they are primarily available, versatile, non-toxic, stable, and biodegradable [21–23]. These proteins exhibit structural domains and functional groups that facilitate the binding with AuNPs, leading to several advantages to pristine AuNPs, including significant internalisation by the organism, longer circulation times, lower toxicity, and selective bio-accumulation [24,25]. Moreover, AuNPs are excellent thermo-optical transducers. Consequently, much work is focused on investigating bio-conjugated AuNPs for photo-thermal therapy (PTT) applications [21,26–28]. PTT is a minimally invasive cancer treatment that can kill tumor cells, mainly through necroptosis and apoptosis mechanisms that occur when the induced temperature is about 43–46 °C [29–31]. Different nanomaterials with excellent photo-thermal properties and high biocompatibility have been used for PTT applications, such as oxide semiconductors [32], semimetals [33], metal-organic [34], and nanofibers [35–37]. Among these nanomaterials, CuS-based NPs are gaining increasing interest as an alternative option to AuNPs [38–41] or combined with plasmonic NPs, which are required to enhance their light-to-heat conversion efficiency [42,43]. However, there are many advantages to using AuNPs due to their easy synthesis and functionalization, low toxicity, stability, and tunable LSPR [44]. Moreover, specific antibodies and proteins can be integrated on the AuNPs' surface, targeting particular cancer sites and actively maximizing cellular uptake [45]. Furthermore, we have already demonstrated [21] that the synthesis of keratin-coated AuNPs (Ker-AuNPs) is easy and fast compared to materials with similar photo-thermal conversion performances, such as oxide semiconductors [32] and metal-organic frameworks [34]. It involves a sustainable approach by using a reduced number of components, all non-toxic and non-hazardous.

However, despite the promising *in vitro* results of suitably bio-conjugated and targeted AuNPs for PTT applications, *in vivo* investigations are still limited by the techniques currently available for localization and detection of AuNPs in the human body.

Indeed, the main techniques are photoacoustic microscopy [46,47], photothermal imaging [48,49], computed tomography [50–52], NIR fluorescence [53,54], and NIR spectroscopy [55,56]. These techniques, although non-invasive, are not able simultaneously to map large regions (in the order of square centimeter) with micrometer resolution. Since many applications in nano-medicine depend on a controllable and efficient delivery of AuNPs to the targeted tissues, a reliable and systematic technique to localize AuNPs requires future developments and optimization.

Combining nuclear medicine imaging techniques with AuNP-based therapeutic approaches offers unique opportunities to achieve this goal. In this framework, radiolabelled AuNPs provide multifold advantages to other photothermal agents. Indeed, Au is a high-Z element; therefore, AuNPs are valuable radio-sensitizers [57,58]. Their plasmonic properties open further benefits, including photoacoustic imaging and surface-enhanced Raman scattering (SERS) [58]. A suitable functionalization of AuNPs is pivotal for merging diagnostic and therapeutic capabilities into a single agent, resulting in the so-called *theranostic* approach. This possibility would require the design of radiolabeled nano-conjugates that possess: a suitable NP geometry, the desired targeting biomolecule, and an optimal imaging or therapeutic radio-nuclide [59–63].

The coordination chemistry approach is widely used to directly bind radioisotopes to the metal NPs surface [64,65]. It is based on

the strong linkage between a chelator agent, such as diethylenetriamine pentaacetic acid (EDTA), and diethylenetriaminepentaacetic acid (DTPA) [66,67], thus coordinating the radioisotope and the NP's surface. This powerful combination assures the chemical and temporal stability of the radiolabeling process [70].

Technetium^{99m}diethylenetriaminepentaacetic acid (^{99m}Tc-DTPA) is the most commonly used radiopharmaceutical for dynamic renal imaging and the least expensive [68,69]. Accordingly, ^{99m}Tc-DTPA conjugated to the NP surface quickly reveals the AuNPs accumulation in tissues using radio-imaging techniques, such as single-photon emission computerized tomography (SPECT) [70–75].

Proof-of-principle experiments to guide future *in vivo* experimental studies to test radiolabeled NPs stability and localization can be performed utilizing lab-on-a-chip (LOC) technology [76,77]. It relies on biomimetic microfluidic devices that mimic several organs, including lungs, liver, and kidneys. LOC technology is valuable tool propaedeutic to *in vivo* experiments, allowing a solid investigation of several medical applications without sacrificing animals [78–82].

One of the most effective approaches to fabricating microfluidic devices is binding micro-channels, molded in a polymer bonded, to a flat surface (such as a glass slide). Polydimethylsiloxane (PDMS) is an optical transparent elastomer primarily used to realize microfluidic chips [80,82]. Moreover, PDMS is biocompatible (similar to silicone gel used in breast implants), deformable, and inexpensive. It has been shown that PDMS can mimic the human kidney tissue in terms of density, flexibility, dielectric constant, and conductivity [82]. These properties demonstrate its excellent suitability as a material to realize a kidney phantom to be used as a LOC for biomedical applications.

This work reports and discusses preparing a new generation of Ker-AuNPs, radiolabeled with the ^{99m}Tc. The radiolabeling of Ker-AuNPs has been accomplished by exploiting the chemical affinity between the keratin and the DTPA molecules chelating the ^{99m}Tc. Keratin provides augmented biocompatibility of the nanoconjugate and facilitates the binding between the ^{99m}Tc-DTPA complex and the AuNP.

A LOC microfluidic-based circuit mimicking the nephron has been designed, fabricated, and used to gain insights into the spatial localization of the ^{99m}Tc-DTPA-Ker-AuNP by the nuclear imaging technique. ^{99m}Tc-DTPA-Ker-AuNPs have been investigated through instant thin-layer chromatography (ITLC), UV–Vis spectroscopy, and a high-resolution thermo-optical setup, revealing a successful photo-conjugation between ^{99m}Tc and Ker-AuNPs along with excellent photo-thermal properties.

The excellent biocompatibility of ^{99m}Tc-DTPA-Ker-AuNPs with healthy human embryonic kidney (HEK) 293 cell line has been demonstrated by monitoring cell proliferation and ultrastructure by transmission electron microscopy (TEM) analysis.

The passive flow of ^{99m}Tc-DTPA-Ker-AuNPs and their temporal-spatial stability inside the nephron-like microfluidic circuit have been studied via spectroscopy, thermo-optical, and SPECT imaging analysis, confirming the extraordinary capability of ^{99m}Tc-DTPA-Ker-AuNPs to be used for PTT-based applications.

2. Materials and method

2.1. Keratin extraction

The protocol used for keratin extraction and AuNPs bio-conjugation was described in Ref. [83]. Here, shortly, we recall that a water solution of keratin was obtained from wool fibers [84]. Wool fibers were first cleaned and rinsed, then dried overnight at room temperature. Keratin was extracted from wool fibers with a

water solution containing 7 M urea, 0.05 M sodium dodecyl sulfate (SDS), and 1.1 M 2-mercaptoethanol. The extraction was performed with 10 g of wool in 180 ml of solution at 60 °C for 5 h. Afterward, the solution was filtered. The resulting solution was centrifuged to remove undissolved fiber residues.

2.2. Synthesis of Ker-AuNPs

AuNPs were synthesized through the Turkevich method [85], using sodium citrate as a reducing agent. The naked AuNPs obtained have a spherical shape with an average diameter of about 30 nm, as confirmed by DLS measurements [21]. A 1.5 mM of Ker-AuNPs and AuNPs solutions were mixed with the keratin solution to have a 1:100 wt ratio between Au and keratin. An amount of keratin three orders of magnitude higher than what was expected to be conjugated was used. This excess of keratin ensured that all the AuNPs binding sites were saturated.

The obtained Ker-AuNPs solution was gently stirred overnight, centrifuged twice at 14,300 rpm to remove free keratin, and finally resuspended in MilliQ water. Using Fourier Transformed Infrared Spectroscopy (FTIR) and X-ray Photoelectron Spectroscopy (XPS) analysis, keratin proteins' presence surrounding AuNPs was already demonstrated [21].

2.3. DTPA-assisted radiolabeling of Ker-AuNPs with ^{99m}Tc

For the radiolabeling of Ker-AuNPs, a chelator-mediated indirect approach was employed. Two agents were used to facilitate the link between the ^{99m}Tc and the Ker-AuNPs: a chelator and a reductant. The chelator, which can link to the AuNP surface and the protein surrounding it, facilitates the conjugation of the radioisotope to the Ker-AuNPs surface. At the same time, the reductant lowers the oxidation number of the radioisotope, increasing its chemical activity. Stannous chloride (SnCl_2) was used as a reducing agent, and diethylenetriaminepentaacetate (DTPA) was employed as a chelator. The pertechnetate ion ($^{99m}\text{Tc O}_4^-$), used as a source of radioisotope, was freshly eluted from Drytec™ Technetium- ^{99m}Tc Generator (GE Health-care, Amersham, UK). SnCl_2 and DTPA were taken from the Technescan DTPA kit for radiopharmaceutical preparation (Mallinckrodt Medical B.V., Netherlands).

As a first step, 20.8 mg of DTPA was reconstituted in 4 ml of saline solution (0.9% NaCl), and 300 μL of this solution was added to 600 μL of Ker-AuNPs water solution 1.5 mM. The DTPA-Ker-AuNPs solution was kept at 37 °C for 15 min. The heating of the solution induced the weakening of the bonds between the keratin amino acids, making the DTPA incorporation easier. As a second step, 0.45 mg of SnCl_2 was reconstituted in a 4 ml saline solution. Freshly eluted sodium pertechnetate (20 μL , 74 Mbq/ml) was reduced by stannous chloride. As a final step, 300 μL of this solution was immediately added to the solution of DTPA-Ker-AuNPs. The final ^{99m}Tc -DTPA-Ker-AuNPs mixture was incubated at room temperature for 15 min after gentle stirring.

2.4. Radiochemical purity (RCP) evaluation via Instant Thin Layer Chromatography (ITLC) and phosphor-based imaging

Instant Thin Layer Chromatography (ITLC) tests were performed to separate the amounts of ^{99m}Tc radioactive impurities from the ^{99m}Tc -DTPA complex and evaluate the radiochemical purity of ^{99m}Tc -DTPA-Ker-AuNPs solution.

ITLC is a separation method of different compounds in a mixture, commonly used to determine the radiochemical purity in nuclear medicine [86]. The migration properties of free pertechnetate and colloidal ^{99m}Tc are influenced by mobile and stationary

phases.

A drop of ^{99m}Tc -DTPA-Ker-AuNPs solution ($\sim 5 \mu\text{l}$) was deposited at the previously marked starting point of three different ITLC plates. The ITLC chambers (Falcon tubes) were filled with the solvent up to 2 cm from their bottom, and the prepared ITLC plates were vertically placed inside each tube, with the deposition spot kept towards the bottom. The chambers were then kept closed. 5–10 min were sufficient for the plates to complete their development, reaching the solvent front. Each plate was immersed in a different mobile phase.

When the development was completed, the amount of radioactive compounds present on the plates was measured with a phosphor imaging instrument (Cyclone Plus, PerkinElmer Analytics). The plates were placed in close contact with a phosphor screen for 20 s so that the radioactivity of the plates could be captured and stored by the screen. The latter was then inserted into a rotating system, and it was scanned point by point using a red laser beam. The signal was transmitted to a high-efficiency PMT and, thanks to a digital processing system, high-resolution (up to 600 dpi) digitized images with quantitative information were obtained.

2.5. Thermo-optical setup

Light-triggered photothermal experiments were performed using the thermo-optical setup illustrated in Fig. 1. A CW green laser (gem532, Laser Quantum), emitting at 532 nm, corresponding to the plasmonic absorption band of the Ker-AuNPs, illuminated the sample in the direction perpendicular to the air/sample interface.

A high-resolution thermal camera was used to map and quantify the temperature profile of the sample's area under laser illumination. The dynamic IR thermographic analysis was carried out using a FLIR (A655sc) thermal-camera (FLIR System, Wilsonville, OR, USA) that produces thermal images of 640x480 pixels with an accuracy of ± 2 °C. The thermal camera was equipped with a close-up IR lens characterized by a magnifying factor of 2.9x, a spatial resolution (IFOV) of 50 μm , and a reduced working distance of 15 cm. A square region of interest (ROI), corresponding to the illuminated area, was selected on thermographic images to measure the maximum and mean temperature values reached in the sample volume. Data collection and analysis were based on carefully evaluating representative IR image sequences acquired during the laser irradiation.

2.6. ^{99m}Tc - DTPA-Ker-AuNPs characterization

2.6.1. Dynamic light scattering and ζ -potential

The hydrodynamic size and ζ -potential of ^{99m}Tc - DTPA-Ker-AuNPs were characterized through dynamic light scattering (DLS)

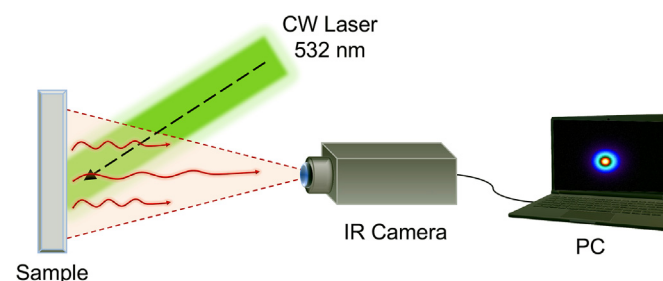


Fig. 1. Schematic representation of the thermo-optical setup used for samples' characterization. A CW laser operating at 532 nm illuminates the sample in the direction perpendicular to the air/sample interface. A high-resolution thermal camera is used to map and quantify the temperature profile of the sample's area under laser illumination.

experiments using a Zeta Sizer NanoZS instrument (Malvern Pan-analytical, Malvern, UK). The ζ -potential was measured between -150 mV and $+150$ mV.

2.6.2. UV–Vis spectroscopy

Absorption spectra were acquired using a UV–Vis spectrophotometer (Lambda 365 from PerkinElmer).

2.6.3. Transmission electron microscopy imaging

TEM images were recorded using a JEOL JEM-1011 apparatus operating at 100 kV. Samples were drop-casted on a Cu grid coated with an ultrathin carbon film previously plasma cleaned. The excess solution was wicked off from the grid's side and was left to dry for at least 24 h before imaging.

2.7. Cell culture

Human Embryonic Kidney 293 T (HEK293T) cells were purchased from American Type Culture Collection (ATCC, CRL-1573, Manassas, VA). The cells were grown following the protocol described in Ref. [87]. Briefly, cells were maintained in Dulbecco's Modified Eagle Medium (DMEM) supplemented with 1% non-essential amino acids, 1% L-glutamine, 100 IU/ml penicillin, 100 IU/ml streptomycin, and 10% Fetal Bovine Serum (FBS, Sigma-Aldrich, St. Louis, MO) at 37 °C in a 5% CO₂-humidified atmosphere. The cells were subcultured only when confluence reached 80%, and the medium was replaced twice a week.

2.8. Cell proliferation assay (MTS)

With some modifications, cell proliferation was evaluated as described in Ref. [88]. 2×10^4 HEK293T cells were seeded into 96-well plates and maintained overnight. Then, cells were exposed to various concentrations of ^{99m}Tc-DTPA-Ker-AuNPs (0–100 μ M) for 24, 48, and 72 h. HEK293T cell proliferation was quantified by MTS–formazan reduction (Promega, Madison, WI) by evaluating the absorbance at 492 nm. Results were indicated as “percentage of proliferation vs. Control.” Three independent experiments were performed in quintuplicate.

2.9. Transmission electron microscopy for ultrastructural cells analysis

HEK293T cells incubated with 100 μ M ^{99m}Tc-DTPA-Ker-AuNPs and Ker-AuNPs for 24 h were detached and transferred to the Eppendorf tubes for TEM processing. After centrifugation, the cell pellet was fixed with 2.5% glutaraldehyde (SIC, Rome, Italy) in 0.1 M PBS for two days at 4 °C and then rinsed with PBS. Afterward, samples were post-fixed using 2% osmium tetroxide (Agar Scientific, Stansted, UK) for 2 h and rinsed again in PBS [89]. The specimens were dehydrated by exchange with ethanol, immersed in propylene oxide (BDH Italia, Milan, Italy) for solvent substitution, and embedded in epoxy resin Embed-812 (SIC, Rome, Italy). Ultrathin (80–90 nm) sections were obtained using an ultramicrotome (Leica EM UC6, Vienna, Austria). For the TEM observation, the ultrathin sections were collected on 100-mesh copper grids (Assing, Rome, Italy) stained with a mix of lanthanides solution (Uranylless, Electron Microscopy Sciences) and lead citrate [90]. Imaging was performed using a transmission electron microscope (Carl Zeiss EM10, Thornwood, NY) with an accelerating voltage of 60 kV and a DEBEN XR80 AMT CCD camera.

2.10. Microfluidic chips fabrication

PDMS replica molding fabricated microfluidic samples and then

bonded on a glass slide by O₂ plasma bonding. The mold was obtained by 3D printing with photocurable materials [91]. In detail, the negative of the geometry of interest was converted into *.STL (Standard Triangulation Language) format and then imported into the 3D printer software. The 3D printer is the Objet30 from Stratasys, and the materials employed are VeroWhite resin and Sup705. The first one is the structural polymer, which shapes the virtual geometry. The accuracy of the printing process was enhanced by the selective deposition of a support material, the Sup705, which helps grow the structure and prevents damage during printing. After the 3D printing process, the mold was cleaned carefully and rinsed with a water jet to remove the support material. The analyzed microfluidic chips have 300 μ m width and 70 μ m height channels. The channels distance varies from 3 to 7 mm.

2.11. SPECT imaging

SPECT imaging measurements were performed using a free-geometry dual-detector gamma camera (Millennium, GE Healthcare, USA), equipped with NaI(Tl) scintillation crystal (thickness = 9.5 mm), 59 circular PMTs (76 mm and 38 mm), NEMA UFOV 40 \times 60 cm, energy range: 40–511 keV.

SPECT imaging of the microfluidic devices was performed with low energy, high resolution (LEHR) collimators, using a 512 \times 512 spatial resolution, 1.5 zooms, with a total acquisition time of 10 min. The single-pixel size is 1.2 \times 0.8 mm.

2.12. Images intensity quantification

Microfluidic chip resolution studies were carried out by analyzing the SPECT images of the microfluidic devices filled with a ^{99m}Tc solution using the ImageJ software.

The software allows obtaining two-dimensional intensity profiles along a selected line across the image. The x-axis represents distance along the line, and the y-axis is the pixel intensity. A line crossing the chip along its short side was used in the actual case.

3. Results and discussion

3.1. Radiochemical purity (RCP) evaluation

A schematic representation of the protocol utilized to prepare ^{99m}Tc-DTPA-Ker-AuNPs, as described in Section 2.3, is reported in Fig. 2.

The complexation of radionuclide and the AuNPs is essential for developing innovative radiotracers. The choice of keratin as a capping agent for AuNPs is fundamental for the augmented biocompatibility of the nanoconjugate and the facilitation of the binding between the ^{99m}Tc-DTPA complex and the AuNP. As already reported in the literature, among the limitations of ^{99m}Tc-DTPA use is that this radiopharmaceutical can bind to many proteins, such as plasma proteins in human blood [92–95]. This binding has significant implications for the kinetics of these substances [94]. In our case, the keratin capping the AuNPs may directly bind to the ^{99m}Tc-DTPA so that, in the light of *in vivo* experiments, the binding site/s of ^{99m}Tc-DTPA turns out to be occupied, thus overcoming plasma proteins binding.

Efforts were made to prepare the ^{99m}Tc-labeled Ker-AuNPs with maximum possible radiochemical purity. The radiolabeling experiments were carried out by varying reaction parameters, such as chelant concentration, reaction time, and incubation temperature.

The radiochemical purity of freshly prepared ^{99m}Tc-DTPA-Ker-AuNPs was investigated by ITLC, which allowed assessing the occurrence of effective radiolabeling.

In general, the preparation of the radiopharmaceutical ^{99m}Tc-

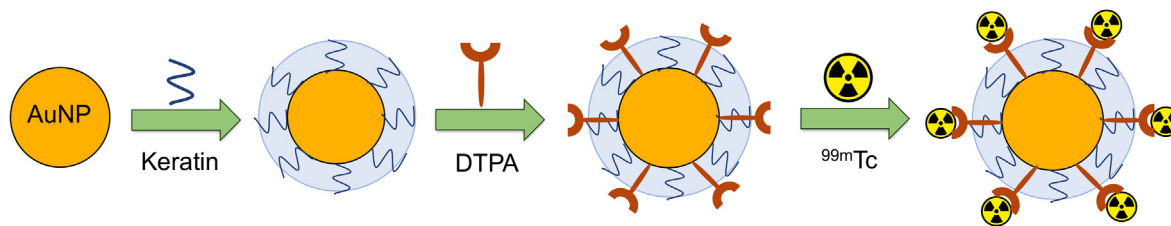


Fig. 2. Schematic of the radiolabeling process to prepare ^{99m}Tc -DTPA-Ker-AuNPs. Spherical AuNPs of approximately 30 nm diameter are coated with keratin using self-assembly techniques. For the radiolabeling process of Ker-AuNPs, a chelator-mediated indirect approach is employed. The chelator (DTPA) links to the Ker-AuNP, facilitating the complexation of the radioisotope (^{99m}Tc) and the NP. ^{99m}Tc was previously reduced to increase its chemical activity.

DTPA may generate radiochemical impurities when the radiolabeling reaction occurs with less than 100% efficiency.

In this case, two different impurities were formed: (i) free ^{99m}Tc O_4^- , i.e., unreduced ^{99m}Tc O_4^- (ii) colloidal ^{99m}Tc species, i.e., technetium oxidised due to undesired contact with air.

Accordingly, when a saline solution (0.9% NaCl) is used as an eluting solvent in an ITLC characterization, free ^{99m}Tc O_4^- and ^{99m}Tc -DTPA complexes migrate up to the end of the ITLC plate. In contrast, ^{99m}Tc colloids remain at the deposition point (indicated as a *start*). In contrast, when using an organic solvent as an eluent (methyl ethyl ketone, or MEK, in our experiment), free ^{99m}Tc O_4^- migrates up to the end of the plate (indicated as a *front*), while the ^{99m}Tc -DTPA complex and the ^{99m}Tc colloids remain at the starting point [86,96]. Finally, using Methanol: Water (80:20) as an eluting solvent, the opposite migration to MEK is obtained. More details can be found in the *Supplementary Information*.

To characterize ^{99m}Tc -DTPA-Ker-AuNPs by ITLC, a drop of the ^{99m}Tc -DTPA-Ker-AuNPs solution ($\sim 5 \mu\text{l}$) was deposited at the previously marked starting point of three different ITLC plates (about 2 cm above the one end of the plates). Afterward, the ITLC plates were immersed in the three mobile phases: the saline solution, the MEK, and a Methanol: Water (80:20) mixture. When the development was completed, the amount of radioactive compounds present at the *start* and at the *front* of the plates was measured via phosphor-based radio imaging techniques. The resulting radiochromatograms are reported in Fig. 3.

Fig. 3a reports the amount of radioactivity expressed in the Density Light Unit (DLU) as a function of the distance and the ITLC plates for each eluent. Each radiochromatogram shows an intense radiochromatographic peak at about 2 cm (corresponding to the starting point) and a broad peak with low intensity at the front of the plate for all the used eluents.

Fig. 3b illustrates the radio images of the three corresponding ITLC plates. Here, a dark, intense spot is present at the starting point

of the three ITLC plates, while a very light stain is visible at the front of the plates.

The radiochromatographic peaks in Fig. 3a and the dark spots in Fig. 3b indicate the presence of strong radioactivity at the starting point of the ITLC plates, where the ^{99m}Tc -DTPA-Ker-AuNPs were deposited. At the same time, only a low percentage of radioactive species migrate to the *front*. Accordingly, it is possible to propose that Ker-AuNPs do not migrate from the starting point of the ITLC plate due to their higher weight if compared with one of the radiochemical impurities. Therefore, the detection of strong radioactivity at the origin of the plate and the resulting negligible amount of radioactive compounds at the *front* provide a qualitative indication that most radioactive species (i.e., the ^{99m}Tc -DTPA complexes) are linked to the Ker-AuNPs, resulting in a ^{99m}Tc -DTPA-Ker-AuNPs nanoconjugate.

Moreover, it was possible to quantify the radioactivity purity of the ^{99m}Tc -DTPA-Ker-AuNPs nanoconjugate by comparing these results with the data obtained from the radiochromatography analysis of free ^{99m}Tc O_4^- , ^{99m}Tc colloids, and ^{99m}Tc -DTPA complexes in the absence of Ker-AuNPs (for more details, see the *Supplementary Information*). As a result, the radiochemical purity of the ^{99m}Tc -DTPA-Ker-AuNPs corresponds to the 90.7% of ^{99m}Tc radioactivity. Such a value approaches the 95% radiochemical purity required for radiopharmaceuticals developed for diagnostic purposes [88]. This result confirms and highlights the successful ^{99m}Tc -labeling of Ker-AuNPs.

3.2. Thermo-optical characterization of the ITLC plates

To confirm that the ^{99m}Tc -DTPA-Ker-AuNPs remain at the deposition site of the ITLC plates, thermo-optical experiments were performed. The experiments aim at identifying the regions of the ITLC strip where Ker-AuNPs are deposited by measuring the heat generated when AuNPs are irradiated with a suitable laser source.

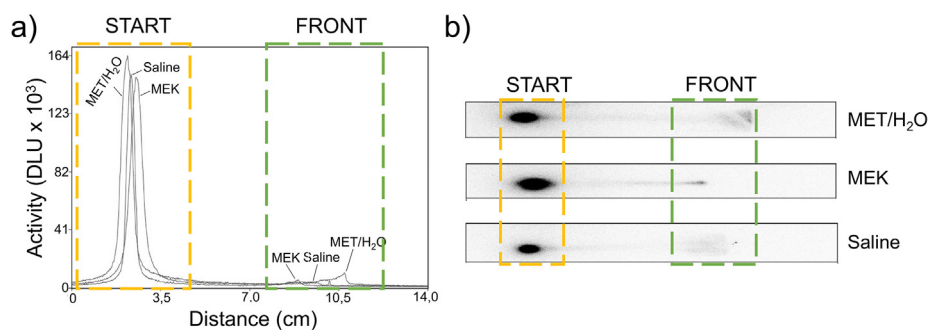


Fig. 3. Phosphor-based radio imaging of the ^{99m}Tc -labeled Ker-AuNPs on ITLC plates. a) Total radiochromatogram profiles of the ^{99m}Tc -labeled Ker-AuNPs obtained with Methanol/Water, MEK, and saline solution as mobile phases. b) Radiochromatograms of ^{99m}Tc -DTPA-Ker-AuNPs solution, obtained after optimized radiolabeling procedure, in methanol/water, MEK, and saline solution as mobile phases.

The ITLC plates were illuminated with a CW green laser emitting at 532 nm and a power density of 3.54 W/cm² in different spots for 2 min. The plate was moved from 0 to 10 cm, with steps of 1 cm. A high-resolution thermographic camera was used to monitor the light-induced temperature changes while scanning the ITLC plates with the laser beam. For simplicity, as similar results were achieved for all three plates, we show in Fig. 4 the thermo-optical characterization of the ITLC plate developed in saline solution. Fig. 4a displays the temperature change measurements as a function of the position of the laser spot on the ITLC plate. Fig. 4b is a photo of the paper strip, where 0 cm indicates the ^{99m}Tc-DTPA-Ker-AuNPs deposition site and 10 cm is the front. A maximum temperature of 58.5 °C is reached (with a photo-thermal efficiency of about 65% [97]) at the deposition site (0 cm). The temperature profile drastically drops to room temperature (~26 °C) when moving the plate 1 cm away. No significant increase in temperature is observed from 1 to 10 cm. Fig. 5c–f report the thermal images of the strips illuminated in different spots, which confirm that when in the presence of ^{99m}Tc-DTPA-Ker-AuNPs, a significant temperature increase was observed. In contrast, the temperature drops to room temperature when moving away from the deposition site. These results confirm that the ^{99m}Tc-DTPA-Ker-AuNPs remain at the starting point of the ITLC plate. As a matter of fact, by combining the thermo-optical analysis and the radiochromatograms (see Section 3.1) of the ITLC plates, it is possible to assess that the ^{99m}Tc-DTPA complex is attached to the Ker-AuNPs and that the ^{99m}Tc-DTPA-Ker-AuNPs nanoconjugates do not migrate from the deposition site, confirming the results reported in Figs. 3 and 4.

3.3. ^{99m}Tc-DTPA-Ker-AuNPs characterization

Further optical, spectroscopic, and morphological studies were performed to demonstrate the modification of the Ker-AuNPs surface associated with the ^{99m}Tc-labeling. Fig. 5a shows the UV–Vis absorption spectra of Ker-AuNPs dispersed in water (orange curve) and the ^{99m}Tc-DTPA-Ker-AuNPs solution (cyan curve). The redshift of the LSPR frequency of approximately 20 nm indicates a variation of the local refractive index surrounding the Ker-AuNPs, which occurred after the radiolabelling step, and an increase in the average radius. Moreover, a broadening of the LSPR peak (FWHM = 65 nm for the orange curve, FWHM = 100 nm for the cyan curve) is noticeable and can be ascribed to an increase of the ^{99m}Tc-DTPA-Ker-AuNPs radius. Indeed, the hydrodynamic diameter

of ^{99m}Tc-DTPA-Ker-AuNPs measured by DLS (Fig. 5b) shows that the average size of the ^{99m}Tc-DTPA-Ker-AuNPs conjugates is approximately 40 nm, thus indicating an increase of the hydrodynamic radius of 33% compared to the as-prepared Ker-AuNPs [21]. To verify that the shift and the broadening of the LSPR band are also attributed to the rise in the ^{99m}Tc-DTPA-Ker-AuNPs radius, we performed control experiments that can be found in the Supplementary Information (Fig. S2).

The successful conjugation between the ^{99m}Tc-DTPA complex and the Ker-AuNPs surface influences the ζ-potential of the Ker-AuNPs. Indeed, Fig. 5c shows that Ker-AuNPs dispersed in water exhibit a ζ-potential of -32.6 ± 1.1 mV (orange curve), whereas ^{99m}Tc-DTPA-Ker-AuNPs show a ζ-potential of -34.5 ± 1.3 mV (cyan curve). The result confirms the change of the chemical environment surrounding the Ker-AuNPs due to the linking with the ^{99m}Tc-DTPA complex while preserving the keratin coating on the AuNPs. This change can probably be associated with the negatively charged carboxylic groups of the ^{99m}Tc-DTPA complex exposed outwards, giving a more negative value of ζ-potential. TEM characterization performed on the ^{99m}Tc-DTPA-Ker-AuNPs solution is shown in Fig. 5d. ^{99m}Tc-DTPA-Ker-AuNPs still exhibit a spherical geometry, with an average diameter of about 30 nm and moderate size distribution. Moreover, a halo around the ^{99m}Tc-DTPA-Ker-AuNPs, a usual indication of the keratin proteins [21], confirms the successful ^{99m}Tc-functionalization.

Notably, the nano-conjugates average diameter measured from the TEM images is lower than the value obtained from DLS measurements. This difference can be explained by considering that the DLS technique provides a hydrodynamic diameter value that considers how NPs diffuse in the fluid and how the NPs scatter laser light. Incorporating the ^{99m}Tc-DTPA complex increases the local refractive index, resulting in an apparent increase in diameter.

It is worth saying that after the ^{99m}Tc-DTPA-Ker-AuNPs solution was left to dry on a copper grid, the TEM analysis was performed (Fig. 5d). The solvent evaporation brings the AuNPs closer to each other, forming possible aggregates. Differently, ^{99m}Tc-DTPA-Ker-AuNPs in solution, as clearly demonstrated in the DLS measurements (see Fig. 5b), do not show aggregates.

3.4. Biocompatibility study of ^{99m}Tc-DTPA-Ker-AuNPs

The MTS assay shown in Fig. 6 evaluates the proliferation of HEK293T cells exposed to increasing concentrations of ^{99m}Tc-DTPA-

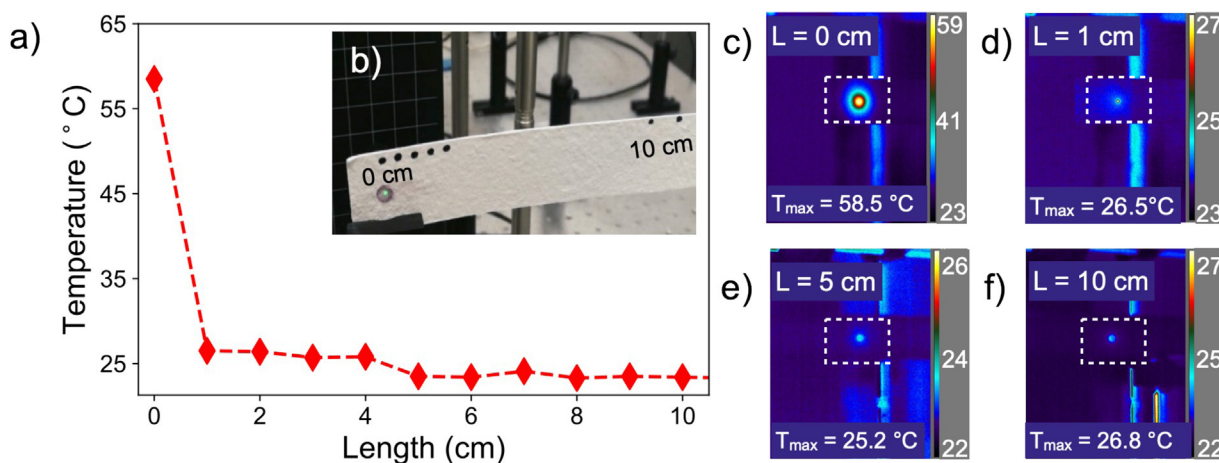


Fig. 4. Thermo-optical analysis of the ITLC plate. a) Spatial-temperature profile measurements. The inset b) shows a photo of the strip, where 0 cm indicates the deposition site and 10 cm the front. A temperature of 58.5 °C is reached at the origin, where the ^{99m}Tc-DTPA-Ker-AuNPs are deposited. A rapid decrease in temperature is observed when moving away from the deposition site. c), d), e), and f) show the thermographic images of the ITLC strip at 0, 1, 5, and 10 cm distances, respectively.

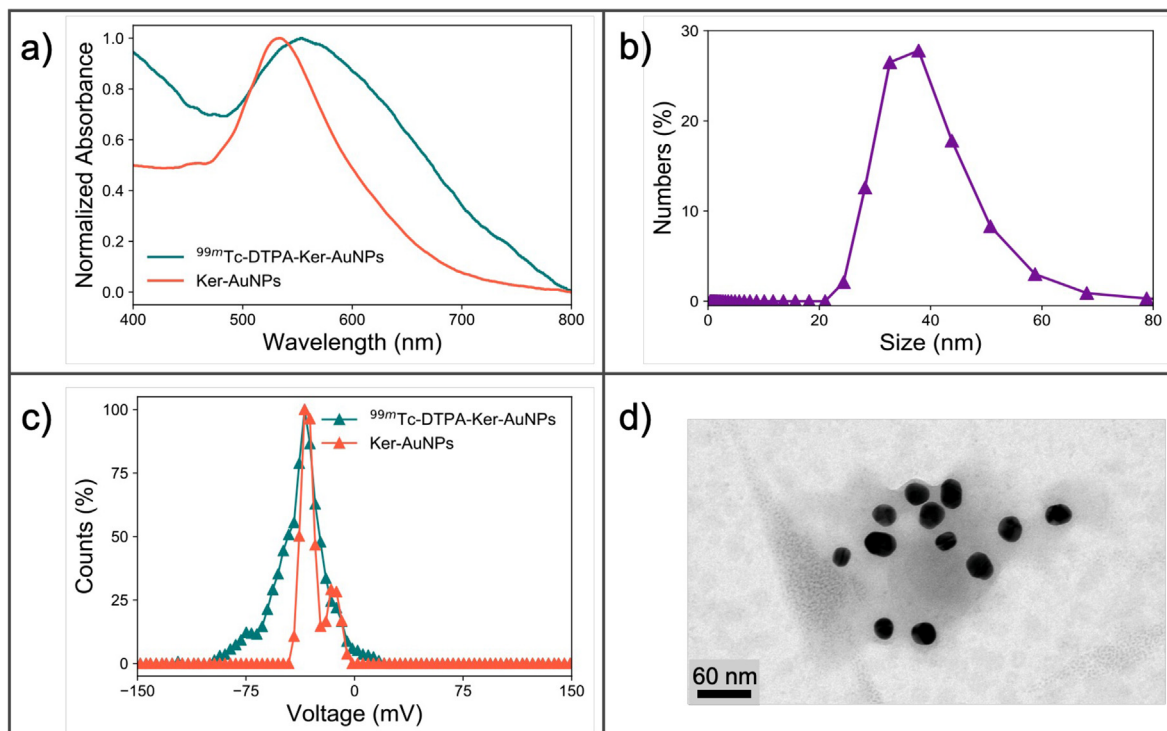


Fig. 5. Ker-AuNPs and ^{99m}Tc -DTPA-Ker-AuNPs characterization. a) Absorption spectra of Ker-AuNPs (orange curve) dispersed in water and of ^{99m}Tc -DTPA-Ker-AuNPs solution (cyan curve). b) DLS measurement of ^{99m}Tc -labeled Ker-AuNPs. c) ζ -potential measurements of the Ker-AuNPs (orange curve) and the ^{99m}Tc -labeled Ker-AuNPs (cyan curve). d) TEM measurement of ^{99m}Tc -labeled Ker-AuNPs.

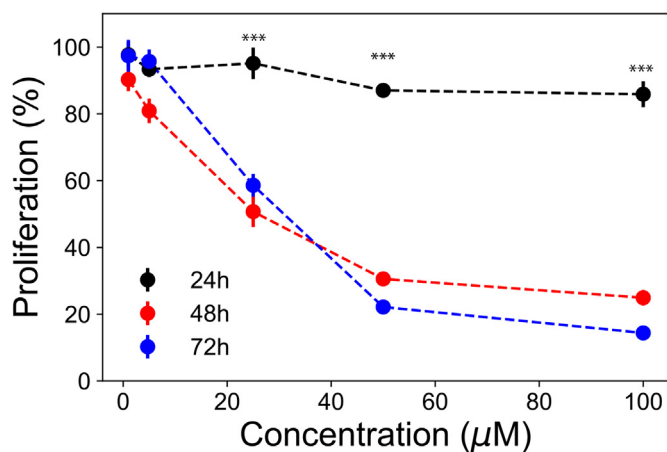


Fig. 6. MTS assay study to check the effects of ^{99m}Tc -DTPA-Ker-AuNPs on the proliferation of HEK293T cells. The results show the proliferation (expressed as percentage vs. control) of HEK293T cells incubated with increasing concentrations (0–100 μM) for 24 h (black curve), 48 h (red curve), and 72 h (blue curve). Results are presented as the mean \pm SD of three independent experiments performed in quintuplicate. The statistical analysis (***: $p < 0.001$) was performed through the statistical test “1-way ANOVA” using the software graph-pad prism v.7.

Ker-AuNPs (0–100 μM) for different incubation times (0–72 h). The administration of ^{99m}Tc -DTPA-Ker-AuNPs for 24 h does not produce any crucial effects on inhibiting the proliferation of HEK293T cells for the concentration range tested. On the contrary, ^{99m}Tc -DTPA-Ker-AuNPs affect the HEK293T cell proliferation when incubated for more than 24 h. More precisely, 100 μM ^{99m}Tc -DTPA-Ker-AuNPs incubated for 48, and 72 h reduce HEK293T cell proliferation by about 75 and 85%, respectively. This observation can be explained by considering that prolonged incubation times (more than 24 h)

might cause cell morphological change, leading to inhibition of proliferation [98]. In light of this evidence, we can assess that a concentration of 100 μM of ^{99m}Tc -DTPA-Ker-AuNPs can be safely employed for photo-thermal treatment without associated side effects if the treatment plane time is well below 24 h.

It is worth pointing out that recent studies have reported that AuNPs conjugated with biocompatible polymers and administrated in a mouse model using intravenous were undetectable in blood 24 h post-administration [99]. Indeed, the biological half-life of AuNPs – based nanoformulations is 10–12 h, and we can safely assume that in 24 h, all the ^{99m}Tc -DTPA-Ker-AuNPs are completely eliminated by the total body clearance. In addition, it is worth remembering that ^{99m}Tc -DTPA has a relatively short physical half-life of 6 h, and its excretion after administration happens during the first twenty-four [100]. For this reason, understanding the mechanism of toxicity caused for prolonged exposure times (>24 h), although very interesting, is out of the scope of this work.

PTT experiments (Supplementary Information, Fig. S4 and Fig. S5) performed with the healthy human embryonic kidney (HEK293T) and the human cell line (U87-MG) derived from glioblastoma, shows a considerable difference in terms of viability reduction. This difference can be explained by considering that cancer cells show more potent thermal cytotoxicity than normal cells. Therefore, we can assess that the photo-thermal properties of ^{99m}Tc -DTPA-Ker-AuNPs affect the cancer cells without being harmful to healthy cells.

3.5. Ultrastructural TEM analysis

Fig. 7 shows the ultrastructural morphology of HEK293T cells incubated with 100 μM ^{99m}Tc -DTPA-Ker-AuNPs for 24 h. The cells tend to move close to each other and have relatively smooth contours with a moderate number of microvilli. Granular cytoplasm containing a large nucleus with a visible nucleolus, cisternae of

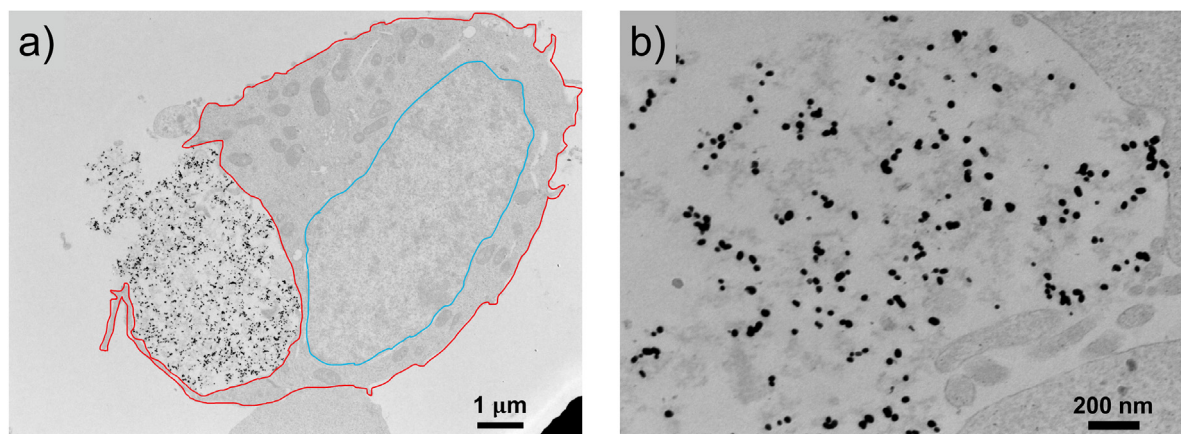


Fig. 7. Ultrastructural morphology of Human Embryonic Kidney 293 T cells incubated with ^{99m}Tc -DTPA-Ker-AuNPs for 24 h. a) shows that the ^{99m}Tc -DTPA-Ker-AuNPs do not penetrate the plasma membrane (red line) of the 293 T cells nor the nucleus (blue line). b) High magnification of the accumulation area of the ^{99m}Tc -DTPA-Ker-AuNPs in the proximity of the plasmatic membrane. The ^{99m}Tc -DTPA-Ker-AuNPs appear to be reasonably monodispersed.

endoplasmic reticulum, and mitochondria are observed (Fig. 7a). Moreover, the TEM analysis of HEK293T cells shows an abundance of mitochondria, where their number, size, and morphology are not altered. Cytoplasmic organelles appear preserved as well. The ^{99m}Tc -DTPA-Ker-AuNPs were not identified inside the cells but densely packed close to the plasma membrane (Fig. 7b), and there were no signs of endocytosis or phagocytosis. From TEM images, we can observe how the cytoplasm and nucleus appear free from AuNPs contamination that remain close to the cells but are not internalized. Despite the ^{99m}Tc -DTPA-Ker-AuNPs treatment, the HEK293T cells showed normal morphology with a preserved ultrastructural arrangement.

Thus, although there is a physical interaction between HEK293T cells and ^{99m}Tc -DTPA-Ker-AuNPs, neither morphological changes, evidence of inflammation, apoptosis, nor necrosis are observed in the cells treated. Therefore, our results indicate that treatments using ^{99m}Tc -DTPA-Ker-AuNPs do not increase cytotoxicity and genotoxicity.

3.6. Towards a dynamic system: lab-on-a-chip approach

The successful radiolabeling of the Ker-AuNPs represents a remarkable result. However, it is mandatory for *in vivo*-oriented applications to check the dynamic stability of ^{99m}Tc -DTPA-Ker-AuNPs to mimic as much stability as possible when they flow through the bloodstream. Indeed, since the NP itself is not radiolabeled, potential detachment of the ^{99m}Tc -DTPA complex from the NP could cause erroneous interpretation of imaging and photo-thermal experiments.

A Lab-on-a-Chip (LoC) approach is proposed to test the spatial-temporal stability of ^{99m}Tc -DTPA-Ker-AuNPs in an *in vivo*-like system without sacrificing animals. Our LoC is based on a simple microfluidic device that consists of a micro-channels net molded in PDMS and bonded to a glass substrate. The micro-channels are connected to two chambers, namely the inlet and the outlet. The inlet injects liquids into the chip, while the outlet allows them to be removed by suction. This way, a “quasi-dynamic” system is obtained to simulate the flow of ^{99m}Tc -DTPA-Ker-AuNPs into micro-channels that resemble human capillaries.

3.7. Resolution studies

The employment of a radio-imaging technique (gamma camera imaging) allows for resolving the microfluidic channels containing

^{99m}Tc -DTPA-Ker-AuNPs. However, it is mandatory to perform preliminary resolution studies to estimate the minimum spatial distance between microfluidic channels. The width of the microfluidic channels and length are the two parameters that need to be carefully chosen to resolve the micro-structure with the gamma camera imaging system.

Fig. 8a shows the drawing of a two-channel geometry system selected to perform resolution studies. The microfluidic chip consists of an inlet, one channel that splits into two arms and re-connections again, and an outlet. The width of each channel is 300 μm , and the height is 70 μm . Three different chips were fabricated, each with an increasing distance between the two arms (3, 5, and 7 mm).

The microfluidic chips were infiltrated with a solution of ^{99m}Tc -DTPA-Ker-AuNPs. Subsequently, gamma camera images were acquired for the 3 mm (Fig. 8b, right panel), the 5 mm (Fig. 8c, right panel), and the 7 mm (Fig. 8d, right panel) spacing. It is possible to observe that a homogeneous distribution of radioactivity is achieved in all three cases. Still, when the capillaries are as close as 3 mm, it is impossible to resolve the chip's structure with micrometric precision.

The plots in Fig. 8 b-d (left panels) show the pixels' intensity values as a function of distance, measured along the dashed white line crossing the chips as shown in the right panels of Fig. 8 b-d. It is possible to observe how the microfluidic channels are not resolved for the 3 mm distancing. In contrast, the channels are well resolved when the distance between them is 5 or 7 mm, with the best result obtained for the latter case.

3.8. Nephron-like microfluidic chip

After optimizing the Ker-AuNPs radiolabeling process and the SPECT imaging parameters for microchannels visualization, a more complex PDMS microfluidic device that mimics a human organ's functionality was implemented. Our choice fell on the kidney's microscopic structural and functional unit, the nephron. The nephron comprises the glomerulus, a dense network of capillaries, and a tubular system [101]. The glomerulus filters the blood flowing from the renal artery. The tubule returns needed substances to the blood in the renal vein through the capillaries system and removes wastes via urine.

AuNPs are likely to be rapidly excreted via the kidneys. However, this effect is mainly size-dependent, as smaller AuNPs (<8 nm) are capable of passing through the renal filtration system. In contrast, larger AuNPs (>10 nm) are more likely to remain in the

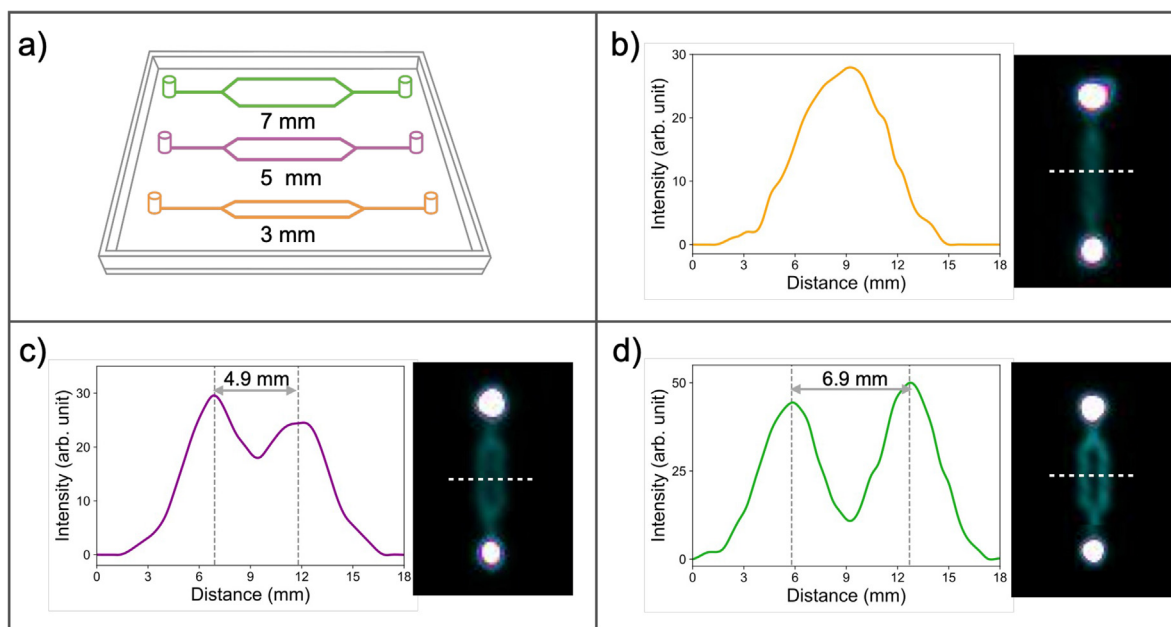


Fig. 8. Resolution study of the microfluidic chip prototype using a gamma camera. a) 3D drawing of the microfluidic prototypes where the width of each channel is $300\ \mu\text{m}$ and the height is $70\ \mu\text{m}$. The distance between capillaries varies from 3 to 7 mm, b), c), and d). Gamma camera images (b, c, d, right) and corresponding intensity profiles (b, c, d, left, obtained along the white dotted lines drawn on the related gamma camera image) of the chip filled with a solution of $^{99\text{m}}\text{Tc}$ -DTPA-Ker-AuNPs.

bloodstream and thus accumulate in the liver and kidney [102,103], as shown in Fig. 9.

On the other hand, after intravenous injection, $^{99\text{m}}\text{Tc}$ -DTPA, the most commonly used radiopharmaceutical for dynamic renal imaging, rapidly diffuses through the extracellular fluid, with peak renal activity reached within 3 min. The complex undergoes blood clearance by glomerular filtration, remains stable *in vivo*, and is excreted unchanged into the urine [96]. The described behaviour indicates a former accumulation of $^{99\text{m}}\text{Tc}$ -DTPA inside the kidney and, in particular, inside the glomerulus, allowing the analysis of kidneys' function and health, as well as the study of the NPs-kidney interaction through SPECT imaging. Moreover, thanks to the light-to-heat conversion ability of AuNPs, $^{99\text{m}}\text{Tc}$ -DTPA-Ker-AuNPs can be investigated for the diagnosis of renal disease and the treatment of kidney cancer. Once the complex is accumulated into the renal

cancer tissue, it can be localized thanks to scintigraphy and can be irradiated by a suitable laser source for efficient heat-mediated destruction of the cancer cells.

For these reasons, a *nephron-like* microfluidic chip was fabricated following the schematic representation shown in Fig. 10a. Fig. 10b illustrates the drawing of the microfluidic chip used in this work. The inlet and the outlet mimic the renal artery and the renal vein. The fluid enters the chip from the inlet, arrives at the glomerulus via the capillaries system, and is finally ejected via the tubule from the outlet. The geometrical parameters of the nephron-like microfluidic channels were properly selected by considering the resolution studies discussed in Section 3.7. The total area of the device is $57\ \text{mm} \times 37\ \text{mm} \times 3\ \text{mm}$. The width of the channels is $300\ \mu\text{m}$, and the distance between them is 7 mm.

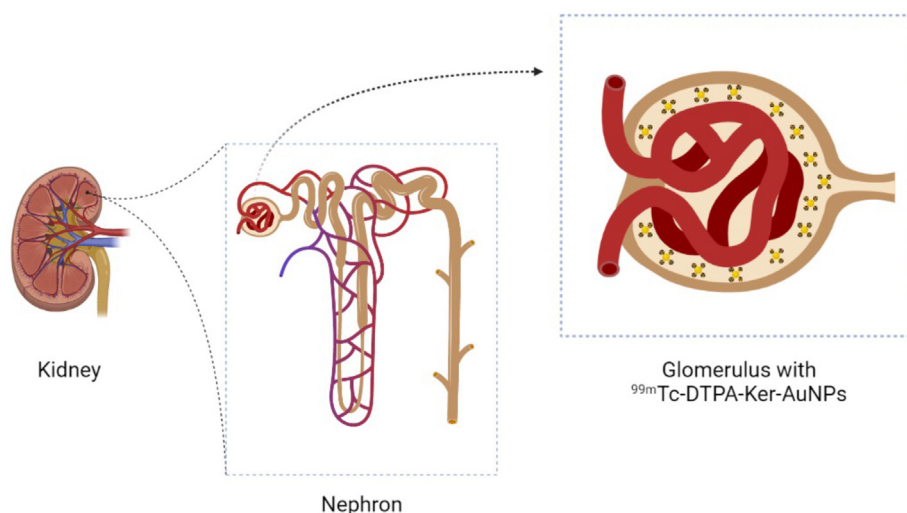


Fig. 9. Schematic reporting the accumulation of $^{99\text{m}}\text{Tc}$ -DTPA-Ker-AuNPs into the kidney.

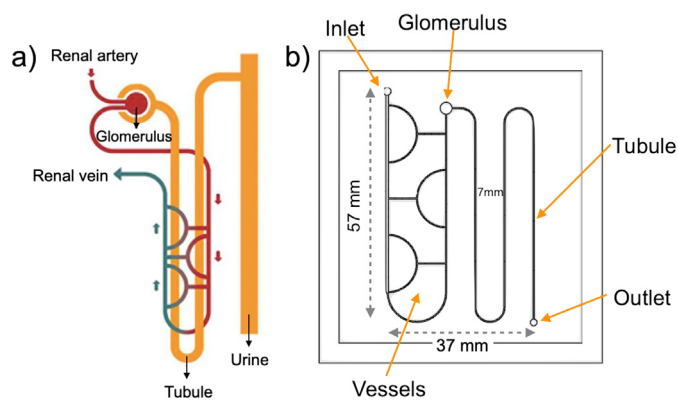


Fig. 10. Nephron-inspired microfluidic chip. a) Schematic representation of a nephron (readapted from National Institute of Diabetes and Digestive and Kidney Diseases, National Institutes of Health). b) Nephron-like PDMS microfluidic chip used in the experiments.

3.9. SPECT imaging of the nephron-like microfluidic chip

The nephron-like microfluidic chip was infiltrated with a ^{99m}Tc -DTPA-Ker-AuNPs solution. The solution was injected into the inlet with a syringe (first step). To simulate the flow of the ^{99m}Tc -DTPA-Ker-AuNPs into the chip, the solution was removed from the outlet by withdrawing the entire content of the chip into a syringe. Successively, the chip was filled for a second time with the same ^{99m}Tc -DTPA-Ker-AuNPs solution (second step). A different chip was filled with a ^{99m}Tc -DTPA solution (third step) as a control experiment. Gamma camera images of the filled chips were acquired at each stage. Fig. 11 shows the results of the SPECT inspection of the chip. At first glance, the microfluidic device's structure appeared pink-

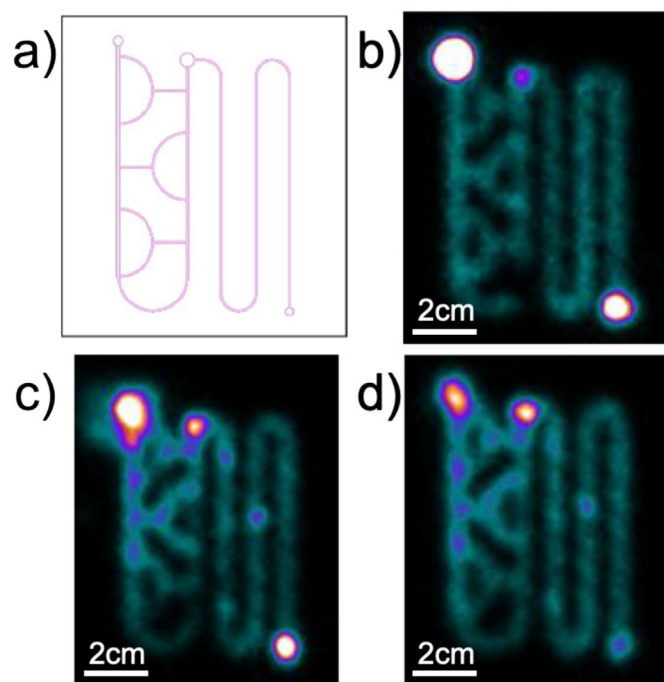


Fig. 11. SPECT imaging experiments of the nephron-like microfluidic chip. a) Schematic of the nephron-like microfluidic chip filled with the ^{99m}Tc -DTPA-Ker-AuNPs solution. b) Gamma camera image of the nephron-like microfluidic chip after a first filling with the ^{99m}Tc -DTPA-Ker-AuNPs solution. c) Gamma camera image was taken after the chip was emptied and filled a second time with the ^{99m}Tc -DTPA-Ker-AuNPs solution. d) Gamma camera image of the chip filled with a ^{99m}Tc -DTPA solution only.

colored, as shown in the schematic representation in Fig. 11a, confirming a homogeneous distribution of ^{99m}Tc -DTPA-Ker-AuNPs inside the channels. Fig. 11b illustrates the gamma camera image taken after the first filling process. It can be observed how the radioactivity distribution is relatively homogeneous inside the capillaries and the tubule of the nephron-like microfluidic chip. However, it is evident that the inlet and the outlet, which are the areas with the highest volumes, present the highest radioactivity concentration. Due to its intermediate volume value, the glomerulus shows a radioactivity distribution between the inlet/outlet and the capillaries cases. Fig. 11c depicts the gamma camera image taken after the second filling step. Also, in this case, a homogeneous distribution of ^{99m}Tc -DTPA-Ker-AuNPs is obtained for the capillaries system while the inlet, the glomerulus, and the outlet show higher radioactivity. Fig. 11d shows the gamma camera image of the sample filled with a ^{99m}Tc -DTPA solution. The radioactivity distribution is similar to the previous cases, despite a few areas that do not show any radioactivity due to the formation of air bubbles into the channel. Given the similarities between ^{99m}Tc -DTPA-Ker-AuNPs and ^{99m}Tc -DTPA, we can conclude that ^{99m}Tc -DTPA-Ker-AuNPs have the same radio-imaging ability as ^{99m}Tc -DTPA while giving the photothermal properties derived from AuNPs.

To check the stability of ^{99m}Tc -DTPA-Ker-AuNPs in a different fluid that mimics a more physiological environment, we have acquired the absorption spectrum of ^{99m}Tc -DTPA-Ker-AuNPs redispersed in a phosphate-buffered saline (PBS) solution. It turns out that (see the *Supplementary Information*, Fig. S5), as it has already demonstrated for Ker-AuNPs [21], the spectral features are retained, thus confirming no sign of aggregation.

3.10. Thermo-optical characterization of the nephron-like microfluidic chip

Once the uniform radioactivity distribution confirmed the presence of radiolabeled Ker-AuNPs in the nephron-like microfluidic chip, photothermal experiments were performed to verify the homogeneous distribution of ^{99m}Tc -DTPA-Ker-AuNPs. This cross-check experiment is devoted to overlapping the uniform radioactivity distribution (confirming the uniform spatial distribution of ^{99m}Tc -DTPA-Ker-AuNPs) and the homogeneous photothermal response (that ensures the uniform spatial distribution of Ker-AuNPs). The sample was irradiated for 2 min in different chip areas, i.e., the inlet, the glomerulus, and the capillary. The thermo-optical setup used for this experiment is reported in Fig. 1. The temperature variations ΔT as a function of time for each area is reported in Fig. 12a. No temperature variations were observed in

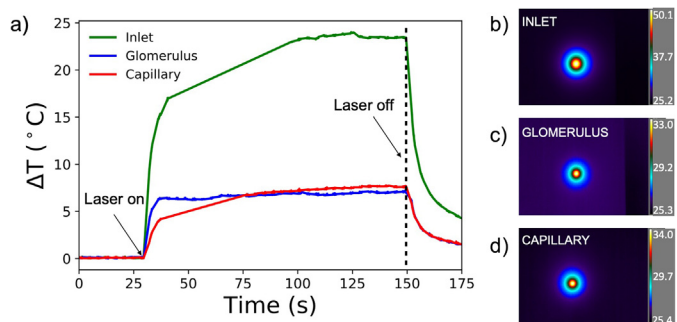


Fig. 12. Thermo-optical analysis of the nephron-like microfluidic chip filled with ^{99m}Tc -DTPA-Ker-AuNPs solution. a) Temperature increment as a function of time measured in different areas of the chip, namely inlet (green curve), glomerulus (blue curve), and capillary (red curve). b), c), and d) show the thermographic images of the three analyzed areas at their maximum temperature.

the first 30 s before illumination started (Laser on). After that, a gradual temperature rise is observed for all three areas; as soon as the laser is switched off (Laser off), each region starts to cool down to the initial temperature. The inlet (green curve) has proven to be the region with the highest temperature increase of about $\Delta T_{MAX} = 24.5$ °C. This result is due to the elevated concentration of ^{99m}Tc -DTPA-Ker-AuNPs in the inlet's volume. In fact, for convenience, both the inlet and the outlet are slightly deeper than the rest of the circuit, making them more significant accumulation areas for the Ker-AuNPs. The glomerulus (blue curve) and the capillary (red curve) show a lower temperature increase, i.e., 8 and 9 °C, respectively. These results are confirmed by the corresponding thermographic images reported in Fig. 12 b-d.

As expected, the smaller amount of ^{99m}Tc -DTPA-Ker-AuNPs solution in the glomerulus and the capillary leads to lower temperature variations ΔT compared to the inlet case. Nevertheless, in the perspective of *in vivo* experiments, a temperature increase of 8–9 °C makes it possible to reach a temperature of about 44–45 °C suitable to destroy cancer cells by regional mild hyperthermia [44]. Moreover, the excellent photo-thermal properties of ^{99m}Tc -DTPA-Ker-AuNPs indicate that they are not aggregate. Indeed, AuNPs aggregation produces negligible photo-thermal heating since all the light gets scattered, thus minimizing the photo-thermal conversion associated with the absorption component [104].

4. Conclusions

We have successfully reported the realization and characterization of novel radiolabeled bio-mimetic AuNPs for PTT-based applications. ^{99m}Tc -DTPA complex, commonly used as a radiopharmaceutical in nuclear medicine, has been employed to radiolabel Ker-AuNPs. The metal chelator (DTPA) facilitates the adhesion of the ^{99m}Tc to the Ker-AuNPs without modifying their biocompatibility, which has been demonstrated by studying their interaction with healthy human cells HEK293T. Ultrastructural TEM analysis allowed us to understand HEK293T morphology, their interaction with ^{99m}Tc -DTPA-Ker-AuNPs, and their uptake mechanisms. A nephron-like PDMS microfluidic device mimics the structure, and the composition of the kidney's filtering unit (the nephron) has been used to study the dynamic stability of ^{99m}Tc -DTPA-Ker-AuNPs. The thermo-optical characterization of the ^{99m}Tc -DTPA-Ker-AuNPs inside the microfluidic device confirmed that, when illuminated by a resonant laser beam ($\lambda = 532$ nm), the AuNPs can still heat up. As such, a temperature increase of 8–9 °C, measured in the glomerulus and capillary, makes it possible to reach a temperature of about 45–46 °C suitable to affect cancer cell viability. Moreover, the presence of the radiolabel linked to the Ker-AuNPs allowed imaging of the spatial distribution of the ^{99m}Tc -DTPA-Ker-AuNPs inside the microfluidic chips using SPECT technique.

The ^{99m}Tc -DTPA-Ker-AuNPs appear to be a promising therapeutic agent acting as multivalent nanoplatforams for imaging and precision nanomedicine applications. In the light of PTT-based applications, future studies are oriented to realize exotic AuNPs (e.g., rods, pyramids, shells, etc.) with higher photo-thermal efficiency and LSPR band in the NIR range (first or second biological windows), where the penetration depth in the tissue is much higher. However, we would like to point out that our work is based on proof-of-concept experiments to demonstrate how a new generation of radiolabeled bio-coated AuNPs can be used as a nano-agent for radio-imaging PTT-applications.

Moreover, it is possible to conjugate ^{99m}Tc -DTPA-Ker-AuNPs with monoclonal antibodies, capable of targeting specific tumor cells and preventing their proliferation. Combining the results obtained in this study and the potential future improvements, a

sophisticated model of PTT against primary tumors can be achieved. This opportunity will produce a selective accumulation of AuNPs to a specific tumor area, enabling active tracking, localizing, and PTT-assisted therapy.

Finally, although our LOC can act as a nephron phantom, we believe that the combination of LOC and human cells, also known as the organ-on-a-chip (OOAC) approach, may be implemented in our future work because it can simulate more precisely the structural and functional characteristics of human tissues. In addition, future experiments will be devoted to including cancer and healthy cells in the same matrix (e.g., via 3D bioprinting) and studying the effect of the temperature increase associated with ^{99m}Tc -DTPA-Ker-AuNPs in a more complex environment. Our finding represents an extraordinary step forward in realizing new drug-free cancer treatments based on the PTT technique.

Authorship statement

V. Frantellizzi: Investigation (performed Radiolabeling experiments and RCP evaluation). V. Verrina: Investigation (performed thermo-optical and spectroscopical experiments), Writing – original draft, Data curation. C. Raso: Investigation (performed thermo-optical and spectroscopical experiments). M. Pontico: Investigation (performed Radiolabeling experiments and RCP evaluation). F. Petronella: Investigation (performed radiolabeling experiments and spectroscopic characterization). V. Bertana: Investigation (Fabrication of the microfluidic chips). A. Ballesio: Investigation (Fabrication of the microfluidic chips). S.L. Marasso: Investigation (Fabrication of the microfluidic chips). S. Miglietta: Investigation (performed ultrastructural TEM analysis). P. Rosa: Investigation (performed cells viability experiments). S. Scibetta: Investigation (performed cells viability experiments). V. Petrozza: Investigation (performed ultrastructural TEM analysis). M.S. De Feo: Investigation (performed Radiolabeling experiments and RCP evaluation). G. De Vincentis: Investigation (performed SPECT imaging experiments). A. Calogero: Investigation (performed cells viability experiments) and conceptualization. R. Pani: Conceptualization. G. Perrotto: Investigation (performed the synthesis and the characterization of the keratin coated gold nanoparticles). L. De Sio: Conceptualization, Investigation (designed the photo-thermal setup), Supervision, Writing-reviewing & editing.

Declaration of competing interest

The authors declare the following financial interests/personal relationships which may be considered as potential competing interests: Luciano De Sio reports financial support and administrative support were provided by University of Rome La Sapienza. Luciano De Sio reports financial support was provided by Lazio Health Regional Health System.

Acknowledgements

This research was supported by the POR FESR LAZIO 2014–2020 - Project T0002E0001 “Photo-thermal cancer therapy based on radio-labeled gold nanoparticles-NANO-TAFT (2020–2022) Grant No 28166”.

Appendix A. Supplementary data

Supplementary data to this article can be found online at <https://doi.org/10.1016/j.mtaadv.2022.100286>.

References

- [1] X. Zhang, Gold nanoparticles: recent advances in the biomedical applications, *Cell Biochem. Biophys.* 72 (2015) 771–775, <https://doi.org/10.1007/s12013-015-0529-4>.
- [2] A. Guglielmelli, F. Pierini, N. Tabiryran, C. Umeton, T.J. Bunning, L. De Sio, Thermoplasmonics with gold nanoparticles: a new weapon in modern optics and biomedicine, *Adv. Photonics Res.* 2 (2021), 2000198, <https://doi.org/10.1002/adpr.202000198>.
- [3] A.J. Mieszawska, W.J.M. Mulder, Z.A. Fayad, D.P. Cormode, Multifunctional gold nanoparticles for diagnosis and therapy of disease, *Mol. Pharm.* 10 (3) (2013) 831–847, <https://doi.org/10.1021/mp3005885>.
- [4] N.S. Aminabad, M. Farshbaf, A. Akbarzadeh, Recent advances of gold nanoparticles in biomedical applications: state of the art, *Cell Biochem. Biophys.* 77 (2) (2019) 123–137, <https://doi.org/10.1007/s12013-018-0863-4>.
- [5] D. Maccora, V. Dini, C. Battocchio, I. Fratoddi, A. Carboni, D. Rotili, M. Castagnola, R. Faccini, I. Bruno, T. Scotognella, A. Giordano, I. Venditti, Gold nanoparticles and nanorods in nuclear medicine: a mini review, *Appl. Sci.* 9 (2019) 3232, <https://doi.org/10.3390/app9163232>.
- [6] A.F. Versiani, L.M. Andrade, E.M.N. Martins, S. Scalzo, J.M. Geraldo, C.R. Chaves, D.C. Ferreira, M. Ladeira, S. Guatimosim, L.O. Ladeira, F.G. da Fonseca, Gold nanoparticles and their applications in biomedicine, *Future Virol.* 11 (4) (2016) 293–309, <https://doi.org/10.1039/C6SC03631G>.
- [7] D. Pissuwan, S.M. Valenzuela, M.B. Cortie, Therapeutic possibilities of plasmonically heated gold nanoparticles, *Trends Biotechnol.* 24 (2) (2006) 62–67, <https://doi.org/10.1016/j.tibtech.2005.12.004>.
- [8] M. Mirrahimi, J. Beik, M. Mirrahimi, Z. Alamzadeh, S. Teymouri, V.P. Mahabadi, N. Eslahi, F.E. Tazehmahalleh, H. Ghaznavi, A. Shakeri-Zadeh, C. Moustakis, Triple combination of heat, drug and radiation using alginate hydrogel co-loaded with gold nanoparticles and cisplatin for locally synergistic cancer therapy, *Int. J. Biol. Macromol.* 158 (2020) 617–626, <https://doi.org/10.1016/j.ijbiomac.2020.04.272>.
- [9] Z. Hua, T. Yu, D. Liu, Y. Xianyu, Recent advances in gold nanoparticles-based biosensors for food safety detection, *Biosens. Bioelectron.* 179 (2021), 113076, <https://doi.org/10.1016/j.bios.2021.113076>.
- [10] S. Siddique, J.C.L. Chow, Gold nanoparticles for drug delivery and cancer therapy, *Appl. Sci.* 10 (2020) 3824, <https://doi.org/10.3390/app10113824>.
- [11] K. Sztandera, M. Gorzkiewicz, B. Klajnert-Maculewicz, Gold nanoparticles in cancer treatment, *Mol. Pharm.* 16 (1) (2019) 1–23, <https://doi.org/10.1021/acs.molpharmaceut.8b00810>.
- [12] T. Curry, R. Kopelman, M. Shilo, R. Popovtzer, Multifunctional theranostic gold nanoparticles for targeted ct imaging and photothermal therapy, *Contrast Media Mol. Imaging* 9 (2014) 53–61, <https://doi.org/10.1002/cmmi.1563>.
- [13] L. De Sio, *Active Plasmonic Nanomaterials*, CRC Press, FL, USA, 2015.
- [14] V. Amendola, R. Pilot, M. Frasconi, O.M. Maragò, M.A. Iatì, Surface plasmon resonance in gold nanoparticles: a review, *J. Phys. Condens. Matter* 29 (2017), 203002, <https://doi.org/10.1088/1361-648x/aa60f3>.
- [15] S.A. Maier, *Plasmonics: Fundamentals and Applications*, Springer US, 2007.
- [16] L. Novotny, B. Hecht, *Principles of Nano-Optics*, Cambridge University Press, 2012.
- [17] P.M. Tiwari, K. Vig, V.A. Dennis, S.R. Singh, Functionalized gold nanoparticles and their biomedical applications, *Nanomaterials* 1 (2011) 31–63, <https://doi.org/10.3390/nano1010031>.
- [18] S.J. Amina, B. Guo, A review on the synthesis and functionalization of gold nanoparticles as a drug delivery vehicle, *Int. J. Nanomed.* 15 (2020) 9823–9857, <https://doi.org/10.2147/IJN.S279094>.
- [19] Y. Wang, J.E.Q. Quinsaat, T. Ono, M. Maeki, M. Tokeshi, T. Isono, K. Tajima, T. Satoh, S. Sato, Y. Miura, T. Yamamoto, Enhanced dispersion stability of gold nanoparticles by the physisorption of Cyclic Poly(Ethylene Glycol), *Nat. Commun.* 11 (2020) 6089, <https://doi.org/10.1038/s41467-020-19947-8>.
- [20] F. Pierini, P. Nakielski, O. Urbanek, S. Pawłowska, M. Lanzi, L. De Sio, T.A. Kowalewski, Polymer-based nanomaterials for photothermal therapy: from light-responsive to multifunctional nanoplatforms for synergistically combined technologies, *Biomacromolecules* 19 (11) (2018) 4147–4167, <https://doi.org/10.1021/acs.biomac.8b01138>.
- [21] A. Guglielmelli, P. Rosa, M. Contardi, M. Prato, G. Mangino, S. Miglietta, V. Petrozza, R. Pani, A. Calogero, A. Athanassiou, G. Perotto, L. De Sio, Biomimetic keratin gold nanoparticle-mediated in vitro photothermal therapy on glioblastoma multiforme, *Nanomedicine* 16 (2) (2021) 121–138, <https://doi.org/10.2217/nnm-2020-0349>.
- [22] C.Y. Flores, E. Achilli, M. Grasselli, Radiation-induced preparation of core/shell gold/albumin nanoparticles, *Radiat. Phys. Chem.* 142 (2018) 6064, <https://doi.org/10.1016/j.radphyschem.2017.02.030>.
- [23] H.R. Barros, M. Kokkinopoulou, I.C. Riegel-Vidotti, K. Landfester, H. Thérien-Aubin, Gold nanocolloid-protein interactions and their impact on β -sheet amyloid fibril formation, *RSC Adv.* 6 (2016) 9411–9420, <https://doi.org/10.1039/C7RA11219J>.
- [24] K. Bolaños, M.J. Kogan, E. Araya, Capping gold nanoparticles with albumin to improve their biomedical properties, *Int. J. Nanomed.* 14 (2019) 6387–6406, <https://doi.org/10.2147/IJN.S210992>.
- [25] J.G. Rouse, M.E. Van Dyke, A review of keratin-based biomaterials for biomedical applications, *Materials* 3 (2) (2010) 999–1014, <https://doi.org/10.3390/ma3020999>.
- [26] L. Shengnan, Y. Wang, C. Shuning, T. Quan, L. Weitong, H. Lingxiao, Q. Tingting, L. Jinfeng, Improvement of gold nanorods in photothermal therapy: recent progress and perspective, *Front. Pharmacol.* 12 (2021), <https://doi.org/10.3389/fphar.2021.664123>.
- [27] S.M. Al-Jawad, A.A. Taha, M.M. Al-Halbosiy, L.F. Al-Barram, Synthesis and characterization of small-sized gold nanoparticles coated by bovine serum albumin (BSA) for cancer photothermal therapy, *Photodiagnosis Photodyn. Ther.* 21 (2018) 201–210, <https://doi.org/10.1016/j.pdpdt.2017.12.004>.
- [28] L. Mocan, C. Matea, F.A. Tabaran, O. Mosteanu, T. Pop, C. Puia, L. Agoston-Coldea, G. Zaharie, T. Mocan, A.D. Buzoianu, C. Iancu, Selective ex vivo photothermal nano-therapy of solid liver tumors mediated by albumin conjugated gold nanoparticles, *Biomaterials* 119 (2017) 33–42, <https://doi.org/10.1016/j.biomaterials.2016.12.009>.
- [29] M.R.K. Ali, Y. Wu, M.A. El-Sayed, Gold-nanoparticle-Assisted plasmonic photothermal therapy advances toward clinical application, *J. Phys. Chem. C* 123 (25) (2019) 15375–15393, <https://doi.org/10.1021/acs.jpcc.9b01961>.
- [30] X. Liu, G. Shan, J. Yu, W. Yang, Z. Ren, X. Wang, X. Xie, H. Chen, X. Chen, Laser heating of metallic nanoparticles for photothermal ablation applications, *AIP Adv.* 7 (2) (2017), 025308, <https://doi.org/10.1063/1.4977554>.
- [31] X. Huang, M.A. El-Sayed, Plasmonic photo-thermal therapy (PPTT), *Alexandria J. Med.* 47 (1) (2011) 1–9, <https://doi.org/10.1016/j.ajme.2011.01.001>.
- [32] N. Yu, Y. Hu, X. Wang, G. Liu, Z. Wang, Z. Liu, Q. Tian, M. Zhu, X. Shi, Z. Chen, Dynamically tuning near-infrared-induced photothermal performances of TiO₂ nanocrystals by Nb doping for imaging-guided photothermal therapy of tumors, *Nanoscale* (2017) 9148–9159, <https://doi.org/10.1039/C7NR02180A>, 9:26.
- [33] N. Yu, Z. Wang, J. Zhang, Z. Liu, B. Zhu, J. Yu, M. Zhu, C. Peng, Z. Chen, Thiol-capped Bi nanoparticles as stable and all-in-one type theranostic nanoagents for tumor imaging and thermoradiotherapy, *Biomaterials* 161 (2018) 279–291, <https://doi.org/10.1016/j.biomaterials.2018.01.047>.
- [34] N. Yu, P. Qiu, Q. Ren, M. Wen, P. Geng, D.K. Macharia, M. Zhu, Z. Chen, Transforming a sword into a knife: persistent phototoxicity inhibition and alternative therapeutic activation of highly-photosensitized phytochlorin, *ACS Nano* 15 (12) (2021) 19793–19805, <https://doi.org/10.1021/acsnano.1c07241>.
- [35] C. Chen, Z. Wu, P. Ding, N. Sun, H. Liu, Y. Chen, Z. Wang, R. Pei, Peptide NGR modified TiO₂ nanofiber substrate for circulating tumor cells capture, *Adv. Fiber Mater.* 2 (2020) 186–193, <https://doi.org/10.1007/s42765-020-00040-0>.
- [36] J. Zhao, W. Cui, Functional electrospun fibers for local therapy of cancer, *Adv. Fiber Mater.* 2 (2020) 229–245, <https://doi.org/10.1007/s42765-020-00053-9>.
- [37] M. Wang, Y. Tan, D. Li, G. Xu, D. Yin, Y. Xiao, T. Xu, X. Chen, X. Zhu, X. Shi, Negative isolation of circulating tumor cells using a microfluidic platform integrated with streptavidin-functionalized PLGA nanofibers, *Adv. Fiber Mater.* 3 (2021) 192–202, <https://doi.org/10.1007/s42765-021-00075-x>.
- [38] Y. Li, W. Lu, Q. Huang, C. Li, W. Chen, Copper sulfide nanoparticles for photothermal ablation of tumor cells, *Nanomedicine* 5 (8) (2010) 1161–1171, <https://doi.org/10.2217/nnm.10.85>.
- [39] A. Riedinger, T. Avellini, A. Curcio, M. Asti, Y. Xie, R. Tu, S. Marras, A. Lorenzoni, S. Rubagotti, M. Iori, P.C. Capponi, A. Versari, L. Manna, E. Seregini, T. Pellegrino, Post-synthesis incorporation of ⁶⁴Cu in CuS nanocrystals to radiolabel photothermal probes: a feasible approach for clinics, *J. Appl. Comput. Sci.* 137 (48) (2015) 15145–15151, <https://doi.org/10.1021/jacs.5b07973>.
- [40] M. Zhou, J. Li, S. Liang, A.K. Sood, D. Lian, C. Li, CuS nanodots with ultrahigh efficient renal clearance for positron emission tomography imaging and image-guided photothermal therapy, *ACS Nano* 9 (7) (2015) 7085–7096, <https://pubs.acs.org/doi/10.1021/acsnano.5b02635>.
- [41] E. Fanizza, R. Mastrogiacono, O. Pugliese, A. Guglielmelli, L. De Sio, R. Castaldo, M. P. Scavo, M. Giancaspro, F. Rizzi, G. Gentile, F. Vischio, L. Carrieri, I. De Pasquale, G. Mandriota, F. Petronella, C. Ingrassio, M. Lavorgna, R. Comparelli, M. Striccoli, M. L. Curri, N. Depalo, NIR-absorbing mesoporous silica-coated copper sulphide nanostructures for light-to-thermal energy conversion, *Nanomaterials* 12 (2022) 2545, <https://doi.org/10.3390/nano12152545>.
- [42] C. Yang, L. Ma, X. Zou, G. Xiang, W. Chen, Surface plasmon enhanced Ag/CuS nanocomposites for cancer treatment, *Can. Nanotechnol.* 4 (2013) 81–89, <https://doi.org/10.1007/s12645-013-0039-2>.
- [43] S.B. Lakshmanan, X. Zou, M. Hossu, L. Ma, C. Yang, W. Chen, Local field enhanced Au/CuS core-shell nanoparticles as efficient photothermal transducer agents for cancer treatment, *J. Biomed. Nanotechnol.* 8 (6) (2012) 883–889, <https://doi.org/10.1166/jbn.2012.1486>.
- [44] B. De Angelis, N. Depalo, F. Petronella, C. Quintarelli, M.L. Curri, R. Pani, Roberto, A. Calogero, F. Locatelli, L. De Sio, Stimuli-responsive nanoparticle-assisted immunotherapy: a new weapon against solid tumours, *J. Mater. Chem. B* 8 (9) (2020) 1823–1840, <https://doi.org/10.1039/C9TB02246E>.
- [45] A. Verma, F. Stellacci, Effect of surface properties on nanoparticle-cell interactions, *Small* 6 (2010) 12–21, <https://doi.org/10.1002/sml.200901158>.
- [46] J.R. Cook, W. Frey, S. Emelianov, Quantitative photoacoustic imaging of nanoparticles in cells and tissues, *ACS Nano* 7 (2) (2013) 1272–1280, <https://doi.org/10.1021/nn304739s>.
- [47] S. Mallidi, T. Larson, J. Tam, P.P. Joshi, A. Karpiouk, K. Sokolov, S. Emelianov, Multiwavelength photoacoustic imaging and plasmon resonance coupling of gold nanoparticles for selective detection of cancer, *Nano Lett.* 9 (8) (2009)

- 2825–2831, <https://doi.org/10.1021/nl802929u>.
- [48] P. Vermeulen, L. Cognet, B. Lounis, Photothermal microscopy: optical detection of small absorbers in scattering environments, *J. Microsc.* 254 (3) (2014) 115–121, <https://doi.org/10.1111/jmi.12130>.
- [49] V.P. Zharov, D.O. Lapotko, Photothermal imaging of nanoparticles and cells, *IEEE J. Sel. Top. Quant. Electron.* 11 (4) (2015) 733–751, <https://doi.org/10.1109/JSTQE.2005.857382>.
- [50] C. Peng, L. Zheng, Q. Chen, M. Shen, R. Guo, H. Wang, X. Cao, G. Zhang, X. Shi, PEGylated dendrimer entrapped gold nanoparticles for IN VIVO blood pool and tumor imaging by computed tomography, *Biomaterials* 33 (4) (2012) 1107–1119, <https://doi.org/10.1016/j.biomaterials.2011.10.052>.
- [51] T. Nakagawa, K. Gonda, T. Kamei, L. Cong, Y. Hamada, N. Kitamura, H. Tada, T. Ishida, T. Aimiya, N. Furusawa, Y. Nakano, N. Ohuchi, X-ray, computed tomography imaging of a tumor with high sensitivity using gold nanoparticles conjugated to a cancer-specific antibody via polyethylene glycol chains on their surface, *Sci. Technol. Adv. Mater.* 17 (1) (2016) 387–397, <https://doi.org/10.1080/14686996.2016.1194167>.
- [52] R. Meir, K. Shamalov, O. Betzer, M. Motiei, M. HorovitzFried, R. Yehuda, A. Popovtzer, R. Popovtzer, C.J. Cohen, Nanomedicine for cancer immunotherapy: tracking cancer-specific T-Cells in vivo with gold nanoparticles and CT imaging, *ACS Nano* 9 (6) (2015) 6363–6372, <https://doi.org/10.1021/acsnano.5b01939>.
- [53] Y. Zhang, J. Qian, D. Wang, Y. Wang, S. He, Multifunctional gold nanorods with ultrahigh stability and tunability for in vivo fluorescence imaging, SERS detection, and photodynamic therapy, *Angew. Chem., Int. Ed.* 52 (4) (2013) 1148–1151, <https://doi.org/10.1002/anie.201207909>.
- [54] F. Meng, J. Wang, Q. Ping, Y. Yeo, Quantitative assessment of nanoparticle biodistribution by fluorescence imaging, revisited, *ACS Nano* 12 (7) (2018) 6458–6468, <https://doi.org/10.1021/acsnano.8b02881>.
- [55] R.T. Zaman, P. Diagaradjane, J.C. Wang, J. Schwartz, N. Rajaram, K.L. Gill-Sharp, S.H. Cho, H.G. Rylander III, J.D. Payne, S. Krishnan, J.W. Tunnell, In vivo detection of gold nanoshells in tumors using diffuse optical spectroscopy, *IEEE J. Sel. Top. Quant. Electron.* 13 (6) (2007) 1715–1720, <https://doi.org/10.1109/jstqe.2007.910804>.
- [56] W.S. Kuo, C.N. Chang, Y.T. Chang, M.H. Yang, Y.H. Chien, S.J. Chen, C.S. Yeh, Gold nanorods in photodynamic therapy, as hyperthermia agents, and in near-infrared optical imaging, *Angew. Chem., Int. Ed.* 49 (15) (2010) 2711–2715, <https://doi.org/10.1002/anie.200906927>.
- [57] G. Song, L. Cheng, Y. Chao, K. Yang, Z. Liu, Emerging nanotechnology and advanced materials for cancer radiation therapy, *Adv. Mater.* 29 (2017), 1700996, <https://doi.org/10.1002/adma.201700996>.
- [58] N. Daems, C. Michiels, S. Lucas, S. Baatout, A. Aerts Gold nanoparticles meet medical radionuclides, *Nucl. Med. Biol.* 100–101 (2021) 61–90, <https://doi.org/10.1016/j.nucmedbio.2021.06.001>.
- [59] V.S. Madamsetty, A. Mukherjee, S. Mukherjee, Recent trends of the bio-inspired nanoparticles in cancer theranostics, *Front. Pharmacol.* 10 (2019) 1264, <https://doi.org/10.3389/fphar.2019.01264>.
- [60] L. Filippi, V. Frantellizzi, A. Chiaravalloti, M. Pontico, M.S. De Feo, F. Corica, M. Montebello, O. Schillaci, G. De Vincentis, O. Bagni, Prognostic and therapeutic applications of positron emission tomography for a personalized approach to metastatic castration-resistant prostate cancer, *Int. J. Mol. Sci.* 22 (6) (2021) 3036, <https://doi.org/10.3390/ijms22063036>.
- [61] S. Same, A. Aghanejad, S. Akbari Nakhjavani, J. Barar, Y. Omid, Radiolabeled theranostics: magnetic and gold nanoparticles, *Bioimpacts* 6 (3) (2016) 169–181, <https://doi.org/10.15171/bi.2016.23>.
- [62] V. Frantellizzi, M. Conte, M. Pontico, A. Pani, R. Pani, G. De Vincentis, New frontiers in molecular imaging with superparamagnetic iron oxide nanoparticles (SPIONs): efficacy, toxicity, and future applications, *Nucl. Med. Mol. Imaging* 54 (2) (2020) 65–80, <https://doi.org/10.1007/s13139-020-00635-w>.
- [63] S. Goel, C.G. England, F. Chen, W. Cai, Positron emission tomography and nanotechnology: a dynamic duo for cancer theranostics, *Adv. Drug Deliv. Rev.* 113 (2017) 157–176, <https://doi.org/10.1016/j.addr.2016.08.001>.
- [64] A. Heuer-Jungemann, N. Feliu, I. Bakaimi, M. Hamaly, A. Alkilany, I. Chakraborty, A. Masood, M.F. Casula, A. Kostopoulou, E. Oh, K. Susumu, M.H. Stewart, L.L. Medintz, E. Stratakis, W.J. Parak, A.G. Kanaras, The role of ligands in the chemical synthesis and applications of inorganic nanoparticles, *Chem. Rev.* 119 (8) (2019) 4819–4880, <https://doi.org/10.1021/acs.chemrev.8b00733>.
- [65] B.M. Essa, A.A. El-Mohty, M.A. El-Hashash, T.M. Sakr, ^{99m}Tc-citrate-gold nanoparticles as a tumor tracer: synthesis, characterization, radiolabeling and in-vivo studies, *Radiochim. Acta* 108 (10) (2020) 809–819, <https://doi.org/10.1515/ract-2019-3208>.
- [66] R. Chakravarty, S. Goel, A. Dash, W. Cai, Radiolabeled inorganic nanoparticles for positron emission tomography imaging of cancer: an overview, *Q. J. Nucl. Med. Mol. Imaging* 61 (2) (2017) 181–204, <https://doi.org/10.23736/S1824-4785.17.02969-7>.
- [67] N. Daems, C. Michiels, S. Lucas, S. Baatout, A. Aerts, Gold nanoparticles meet medical radionuclides, *Nucl. Med. Biol.* 100–101 (2021) 61–90, <https://doi.org/10.1016/j.nucmedbio.2021.06.001>.
- [68] P. Xie P, J.M. Huang, X.M. Liu, W.J. Wu, L.P. Pan, H.Y. Lin, (^{99m}Tc-DTPA renal dynamic imaging method may be unusable to be used as the reference method in investigating the validity of CDK-EPI equation for determining glomerular filtration rate, *PLoS One* 8 (5) (2013), 62328, <https://doi.org/10.1371/journal.pone.0062328>.
- [69] Y. Wang, M. Li S. Dai, Y. Li, The role of Tc-^{99m} DTPA renal dynamic scintigraphy in retroperitoneal liposarcoma, *BioMed Res. Int.* 2020 (2020), 9765162, <https://doi.org/10.1155/2020/9765162>.
- [70] W. Chao, J. Zhang, S. Li, K. Lu, Evaluation of renal function by ^{99m}Tc-DTPA renal dynamic imaging in different stages of polycystic kidney disease, *J. Nucl. Med.* 59 (2018) 381, https://jnm.snmjournals.org/content/59/supplement_1/381.
- [71] A. Polyak, T.L. Ross, Nanoparticles for SPECT and PET imaging: towards personalized medicine and theranostics, *Curr. Med. Chem.* 25 (34) (2018) 4328–4353, <https://doi.org/10.2174/0929867324666170830095553>.
- [72] S. Wen, L. Zhao, Q. Zhao, D. Li, C. Liu, Z. Yu, M. Shen, J.P. Majoral, S. Mignani, J. Zhao, X. Shi, A promising dual mode SPECT/CT imaging platform based on ^{99m}Tc-labeled multifunctional dendrimer-entrapped gold nanoparticles, *J. Mater. Chem. B* 5 (2017) 3810–3815, <https://doi.org/10.1039/C7TB00543A>.
- [73] M. Felber, M. Bauwens, J.M. Mateos, S. Imstef, F.M. Mottaghy, R. Alberto, ^{99m}Tc radiolabeling and biological evaluation of nanoparticles functionalized with a versatile coating ligand, *Chem. Eur. J.* 21 (2015) 6090–6099, <https://doi.org/10.1002/chem.201405704>.
- [74] A. Gupta, R. Mathur, S. Singh, N. Bag, U.A. Khan, F.J. Ahmad, G.A. Gabr, P. Kesharwani, G.K. Jain, ^{99m}Tc-Methionine gold nanoparticles as a promising biomaterial for enhanced tumor imaging, *J. Pharmacol. Sci.* 110 (2) (2021) 888–897, <https://doi.org/10.1016/j.xphs.2020.11.008>.
- [75] E. Forte, D. Fiorenza, E. Torino, A. Costagliola di Polidoro, C. Cavaliere, P.A. Netti, M. Salvatore, M. Aiello, Radiolabeled PET/MRI nanoparticles for tumor imaging, *J. Clin. Med.* 9 (1) (2019) 89, <https://doi.org/10.3390/jcm9010089>.
- [76] J. Merrin, Frontiers in microfluidics, a teaching resource review, *Bioengineering* 6 (4) (2019) 109, <https://doi.org/10.3390/bioengineering6040109>.
- [77] A.-G. Niculescu, C. Chircov, A.C. Birca, A.M. Grumezescu, Fabrication and applications of microfluidic devices: a review, *Int. J. Mol. Sci.* 22 (4) (2021) 2011, <https://doi.org/10.3390/ijms22042011>.
- [78] N.S. Ha, S. Sadeghi, R.M. van Dam, Recent progress toward microfluidic quality control testing of radiopharmaceuticals, *Micromachines* 8 (11) (2017) 337, <https://doi.org/10.3390/mi8110337>.
- [79] S. Damiati, U.B. Kompella, S.A. Damiati, R. Kodzius, Microfluidic devices for drug delivery systems and drug screening, *Genes* 9 (2) (2018) 103, <https://doi.org/10.3390/genes9020103>.
- [80] S.B. Campbell, Q. Wu, J. Yazbeck, C. Liu, S. Okhovtarian, M. Radisic, Beyond Polydimethylsiloxane: alternative materials for fabrication of Organ-on-a-chip devices and microphysiological systems, *ACS Biomater. Sci. Eng.* 7 (2021), 28802899, <https://doi.org/10.1021/acsbmaterials.0c00640>.
- [81] H. Kimura, Y. Sakai, T. Fujii, Organ/body-on-a-chip based on microfluidic technology for drug discovery, *Drug Metabol. Pharmacokinet.* 33 (1) (2018) 43–48, <https://doi.org/10.1016/j.dmpk.2017.11.003>.
- [82] K. Izdihar, H.R. Abdul Razak, N. Supion, M.K.A. Karim, N.H. Osman, M. Norkhairunnisa, Structural, mechanical, and dielectric properties of polydimethyl-siloxane and silicone elastomer for the fabrication of clinical-grade kidney phantom, *Appl. Sci.* 11 (2021) 1172, <https://doi.org/10.3390/app11031172>.
- [83] G. Perotto, G. Sandri, C. Pignatelli, G. Milanese, A. Athanassiou, Water-based synthesis of keratin micro- and nanoparticles with tunable mucoadhesive properties for drug delivery, *J. Mater. Chem. B* 7 (2019) 4385–4392, <https://doi.org/10.1039/C9TB00443B>.
- [84] K. Yamauchi, A. Yamauchi, T. Kusunoki, A. Kohda, Y. Konishi, Preparation of stable aqueous solution of keratins, and physicochemical and bio-degradational properties of films, *J. Biomed. Mater. Res.* 31 (4) (1996) 439–444, [https://doi.org/10.1002/\(SICI\)1097-4636\(199608\)31:4<439::AID-JBM1>3.0.CO;2-M](https://doi.org/10.1002/(SICI)1097-4636(199608)31:4<439::AID-JBM1>3.0.CO;2-M).
- [85] J. Kimling, M. Maier, B. Okenve, V. Kotaidis, H. Ballot, A. Plech, Turkevich method for gold nanoparticle synthesis revisited, *J. Phys. Chem. B* 110 (32) (2006) 15700–15707, <https://doi.org/10.1021/jp061667w>.
- [86] I. Zolle, *Technetium-^{99m} Pharmaceuticals: Preparation and Quality Control in Nuclear Medicine*, Springer Berlin Heidelberg, 2007.
- [87] D. Ponti, D. Bastianelli, P. Rosa, L. Pacini, M. Ibrahim, E.A. Rendina, G. Ragona, A. Calogero, The expression of B23 and EGR1 proteins is functionally linked in tumor cells under stress conditions, *BMC Cell Biol.* 16 (2015) 27, <https://doi.org/10.1186/s12860-015-0073-5>.
- [88] A. Carducci, G. Scafetta, C. Siciliano, R. Carnevale, P. Rosa, A. Coccia, G. Mangino, A. Bordin, E.M. Vingolo, L. Pierelli, E. Lendaro, G. Ragona, G. Frati, E. De Falco, GMP-grade platelet lysate enhances proliferation and migration of Tenon fibroblasts, *Front. Biosci.* 8 (1) (2016) 84–99, <https://doi.org/10.2741/E753>.
- [89] A. Vitalone, A. Di Sotto, C.L. Mammola, R. Heyn, S. Miglietta, P. Mariani, F. Sciubba, F. Passarelli, P. Nativio, G. Mazzanti, Phytochemical analysis and effects on ingestive behaviour of a Caralluma fimbriata extract, *Food Chem. Toxicol.* 108 A (2017) 63–73, <https://doi.org/10.1016/j.fct.2017.07.027>.
- [90] M. Relucenti, S. Miglietta, G. Bove, O. Donfrancesco, E. Battaglione, P. Familiari, C. Barbaranelli, E. Covelli, M. Barbara, G. Familiari, SEM BSE 3D Image Analysis of Human Incus Bone Affected by Cholesteatoma Ascribes to Osteoclasts the Bone Erosion and VpSEM dEDX Analysis Reveals New Bone Formation, 2020, 9371516, <https://doi.org/10.1155/2020/9371516>.
- [91] M. Segantini, M. Parmeggiani, A. Balleisio, G. Palmara, F. Frascella, S.L. Marasso, M. Cocuzza, Design of a portable microfluidic platform for egot-based in liquid biosensing, *Sensors* 22 (3) (2022) 969, <https://doi.org/10.3390/s22030969>.
- [92] F. Maisano, L. Gozzini, C. De Haen, Coupling of DTPA to proteins: a critical

- analysis of the cyclic dianhydride method in the case of insulin modification, *Bioconjugate Chem.* 3 (3) (1992) 212–217, <https://doi.org/10.1021/bc00015a002>.
- [93] N. Vanlić-Razumenić, J. Joksimović, B. Ristić, M. Tomić, S. Beatović, B. Ajdinović, Interaction of ^{99m}Tc -radiopharmaceuticals with transport proteins in human blood, *Nucl. Med. Biol.* 20 (1993) 363–365, [https://doi.org/10.1016/0969-8051\(93\)90060-8](https://doi.org/10.1016/0969-8051(93)90060-8).
- [94] M. Rehling, L.E. Nielsen, J. Marquersen, Protein binding of $^{99\text{Tc}}$ -DTPA compared with other GFR tracers, *Nucl. Med. Commun.* 22 (6) (2001) 617–623, <https://doi.org/10.1097/00006231-200106000-00003>.
- [95] L. Chemlal, J. Akachar, S. Makram, B. Zoubir, Y. Cherrah, R. Eljaoudi, A. Ibrahim, M.A. Faouzi, The displacement study of ^{99m}Tc -DTPA-Human serum albumin binding in presence of furosemide and metformin by using equilibrium dialysis and molecular docking, *IUBMB Life* 71 (2019) 2003–2009, <https://doi.org/10.1002/iub.2167>.
- [96] *Radiopharmacy Eanm, An Update. A Technologist's Guide, European Association of Nuclear Medicine, Vienna, Austria, 2019.*
- [97] N. Yu, W. Tu, P. Qiu, Q. Ren, X. Chen, M. Zhu, Y. Liu, Z. Chen, Full-route advances via biomimetic and biodegradable ultrasmall-in-nano architectures with radiation-photo synergy, *Nano Today* 43 (2022), 101427, <https://doi.org/10.1016/j.nantod.2022.101427>.
- [98] P. Zhao, X. Chen, Q. Wang, H. Zou, Y. Xie, H. Liu, Y. Zhou, P. Liu, H. Dai, Differential toxicity mechanism of gold nanoparticles in HK-2 renal proximal tubular cells and 786-0 carcinoma cells, *Nanomedicine* 15 (11) (2020) 1079–1096, <https://doi.org/10.2217/nmm-2019-0417>.
- [99] A.L. Bailly, F. Correard, A. Popov, G. Tselikov, F. Chaspoul, R. Appay, A. Al-Kattan, A.V. Kabashin, D. Braguer, M.A. Esteve, *In vivo* evaluation of safety, biodistribution and pharmacokinetics of laser-synthesized gold nanoparticles, *Sci. Rep.* 9 (2019), 12890, <https://doi.org/10.1038/s41598-019-48748-3>.
- [100] P.V. Harper, K.A. Lathrop, F. Jiminez, R. Fink, A. Gottschalk, Technetium 99m as a scanning agent, *Radiology* 85 (1) (1965) 101–109, <https://doi.org/10.1148/85.1.101>.
- [101] V.G. Puelles, A.N. Combes, J.F. Bertram, Clearly imaging and quantifying the kidney in 3D, *Kidney Int.* 100 (4) (2021) 780–786, <https://doi.org/10.1016/j.kint.2021.04.042>.
- [102] M. Bartneck, H.A. Keul, M. Wambach, J. Bornemann, U. Gbureck, N. Chatain, S. Neuss, F. Tacke, J. Groll, G. Zwadlo-Klarwasser, Effects of nanoparticle surface-coupled peptides, functional endgroups, and charge on intracellular distribution and functionality of human primary reticuloendothelial cells, *Nanomed. Nanotechnol. Biol. Med.* 8 (8) (2012) 1282–1292, <https://doi.org/10.1016/j.nano.2012.02.012>.
- [103] E. Blanco, H. Shen, M. Ferrari, Principles of nanoparticle design for overcoming biological barriers to drug delivery, *Nat. Biotechnol.* 33 (2015) 941–951, <https://doi.org/10.1038/nbt.3330>.
- [104] L. De Sio, T. Placido, R. Comparelli, M.L. Curri, M. Striccoli, N. Tabiryan, T.J. Bunning, Next-generation thermo-plasmonic technologies and plasmonic nanoparticles in optoelectronics, *Prog. Quant. Electron.* 41 (2015) 23–70, <https://doi.org/10.1016/j.pquantelec.2015.03.001>.